

1 **Revision 3**

2

3 **New insights into the control of visible gold**
4 **fineness and deposition: A case study of the**
5 **Sanshandao gold deposit (Jiaodong, China)**

6

7 Hong-Wei Peng^{1,2}, Hong-Rui Fan^{1,2,3*}, Xuan Liu⁴, Bo-Jie Wen⁵, Yong-Wen
8 Zhang^{1,2}, Kai Feng^{1,2}

9

10 *¹Key Laboratory of Mineral Resources, Institute of Geology and Geophysics,*
11 *Chinese Academy of Sciences, Beijing 100029, China*

12 *²College of Earth and Planetary Sciences, University of Chinese Academy of*
13 *Sciences, Beijing 100049, China*

14 *³Innovation Academy for Earth Science, Chinese Academy of Sciences,*
15 *Beijing 100029, China*

16 *⁴GeoRessources Lab, Université de Lorraine, CNRS, CREGU, 54500*
17 *Vandoeuvre-lès-Nancy, France*

18 *⁵Institute of Mineral Resources, Chinese Academy of Geological Sciences,*
19 *Beijing 100037, China*

20 *Corresponding author. E-mail: fanhr@mail.iggcas.ac.cn; Address: as above;
21 Phone: (+86) 010 82998218; Fax: (+86) 10 62010846

ABSTRACT

22

23 Mineralogical distribution, textures, electron probe microanalysis of visible
24 gold, laser ablation inductively coupled plasma mass spectrometry (LA-ICP-
25 MS) trace element analysis of pyrite, and LA-multicollector (MC-)ICP-MS
26 sulfur isotope analysis of sulfide minerals are examined in an ore zone
27 extending obliquely to -4 km depth in the Sanshandao gold deposit (Jiaodong,
28 China). We relate these results to the temporal and spatial ore forming processes
29 in the deposit to further elucidate the controls on deposition of visible Au and
30 fineness variation.

31 Two generations of Au mineralization are identified. The early generation
32 is represented by beresitization and quartz-pyrite veins, in which visible Au
33 grains are associated with pyrite (Py1 and Py2) and are characterized by high
34 fineness (729-961; fineness = $1000 \times \text{Au}/(\text{Au} + \text{Ag})$). Py1 and Py2 are both
35 enriched in Co, Ni and Bi, and depleted in As and Au. Texturally, gold and pyrite
36 are pristine crystals, homogeneous in composition. These features are attributed
37 to the sulfidation of the granitic wallrock (fluid rock interaction) that effectively
38 destabilizes Au in the ore forming fluids during pyrite deposition. Fineness
39 decreases continuously from 870 at -2650 m depth to 752 at -420 m depth. The
40 Co and Ni contents of Py1 and Py2 decrease significantly from -4000 m to -420
41 m depth, whereas the As contents increase. The mean $\delta^{34}\text{S}$ values of Py1
42 increase from 10.5‰ to 11.8‰. The spatial variations are interpreted to be
43 related to gradual cooling, decompression and an enhanced degree of fluid/rock

44 interaction with decreasing depth, which facilitated the initiation of visible gold
45 mineralization at ca. -2700 m depth.

46 The late generation of Au mineralization is represented by quartz-
47 polysulfide veins, in which visible Au grains are associated with multiple
48 sulfide minerals (Py₃, galena, chalcopyrite, arsenopyrite and sphalerite). It is
49 characterized by low fineness (549-719), and heterogeneous textures with Ag-
50 rich parts (218-421). Py₃, occurring as the rim of pyrite grain are interpreted to
51 form by replacement via a dissolution-reprecipitation reaction. Py₃ is distinctly
52 enriched in As (median of 10000 ppm) and Au (2.2 ppm), but depleted in Co,
53 Ni and Bi. The $\delta^{34}\text{S}$ values of the polysulfide minerals decrease sharply by 4 to
54 5‰ at depths from -1909 to -1450 m depth. These features are interpreted to be
55 generated by significant decompression and phase separation of fluid, where
56 most ore elements (e.g. Au, Ag, As and base metal elements) are destabilized.
57 Our study suggests that remobilization did not affect the generation of visible
58 Au mineralization at Sanshandao.

59 **Keywords:** visible gold grain; fineness; *in-situ* pyrite trace elements; *in-situ*
60 sulfide sulfur isotope; Sanshandao gold deposit; Jiaodong

INTRODUCTION

61

62 Visible Au, the product of Au super-saturation in ore-forming fluid, is the
63 primary and crucial resource of Au in different types of Au deposits. There is
64 complete Au-Ag solid solution and the composition is normally expressed as
65 the Au fineness (1000 Au/(Au + Ag), by weight; Hough et al. 2009). The Au
66 fineness shows different ranges in different deposits (Morrison et al. 1991), and
67 was deemed to be an indicator of the ore-forming process (Pal'yanova 2008).
68 In recent years, many attempts have been made to understand what factors
69 control deposition and fineness of Au by physicochemical modeling, and it has
70 been found to be complicatedly related to multiple-physicochemical conditions
71 (Morrison et al. 1991; Gammons and Williams-Jones 1995; Pal'yanova 2008;
72 Liang and Hoshino 2015). This complexity makes it difficult to directly
73 correlate the Au fineness with the ore-forming process, and the factors which
74 control the Au fineness range and variation in a deposit are poorly constrained.
75 Numerous studies have proposed the crucial role of remobilization in
76 concentrating Au sources and forming visible Au grains (e.g. Morey et al. 2008;
77 Large et al. 2009, 2011; Sung et al. 2009; Cook et al. 2013; Fougereuse et al.
78 2016; and references therein). However, although remobilization is thought to
79 be commonplace in Au deposits, its ability to produce the majority of observed
80 features of visible Au is still in question.

81 Gold in a majority of deposits shows close temporal and spatial
82 relationship with sulfide minerals, especially (arsenian) pyrite (Large et al. 2011;

83 Deditius et al. 2014; Kusebauch et al. 2019; and references therein). The co-
84 occurrence with Au makes pyrite a good proxy for Au deposition processes.
85 Pyrite composition and texture have been used to trace mineralization history
86 and related physicochemical conditions in Au deposits (Morey et al. 2008;
87 Large et al. 2009, 2011; Cook et al. 2013; Gregory et al. 2016; Román et al.
88 2019; and references therein). Specifically, the sulfur isotopic composition of
89 sulfides can reflect the depositional condition of Au (e.g. f_{O_2} and pH; Ohmoto
90 1972; Seal 2006), as Au in hydrothermal solution is commonly transported as
91 sulfide complexes of $AuHS^0$ and $Au(HS)_2^-$ (Benning and Seward 1996;
92 Stefansson and Seward 2003; Williams-Jones et al. 2009). Here, we combine
93 textural and geochemical information of pyrite and other sulfide minerals with
94 fineness of visible Au grains to determine what processes and factors control
95 the deposition and fineness variation of Au.

96 The Jiaodong Au district, containing more than 4000 t Au resources, is the
97 largest and most important Au producing region in China (Zhu et al. 2015; and
98 references therein). In the region, the two major types of Au deposit,
99 disseminated- and quartz vein-type, are both characterized by visible Au
100 mineralization. However, little attention has been paid to the ore-forming
101 process responsible for the visible Au mineralization. Recently, *in situ* analyses
102 of pyrite in quartz vein-type Au deposits have revealed coupled behavior of As
103 and Au (As-poor and As-rich; Feng et al. 2018; Li et al. 2018), which contrasts
104 with the invariant trace element patterns in disseminated-type deposit (Yang et

105 al. 2016), indicating different ore-forming events in Jiaodong.

106 The Sanshandao Au deposit is one of the largest disseminated-type deposit
107 in Jiaodong. The existence of arsenopyrite at shallow level (ca. <-1000 m depth;
108 Fan et al. 2003) suggests As-rich fluids, and may imply the two types of ore-
109 forming mechanisms at this deposit. Recently, deep drill holes (deepest down
110 to -4006.17 m) have revealed visible Au mineralization with large-tonnage
111 sources (totaling more than 1000 t) extending obliquely downward along the
112 ore-controlling fault (Song et al. 2019). The lack of arsenopyrite in deep
113 samples (Zhang et al. 2014) suggests important spatial variation in mineralogy
114 and geochemistry of the deposit. Hence, the Sanshandao Au deposit provides
115 an excellent opportunity to investigate the integrated temporal and spatial ore-
116 forming processes, and further provides key information on the processes and
117 factors required for the deposition of large scale visible Au mineralization in the
118 Sanshandao deposit and Jiaodong Au district.

119

120 THE SANSHANDAO DEPOSIT

121 The Sanshandao Au deposit is located in the west of the Jiaodong
122 Peninsula, which is one of the most important Au-producing area in China,
123 situated in the southeast margin of the North China Craton (Fig. 1a). The
124 geology of the Jiaodong Au district is mainly comprised of Precambrian
125 metamorphic basement rocks and three generations of Mesozoic magmatic
126 intrusions including the late Jurassic Linglong biotite granites (160-150 Ma),

127 the early Cretaceous Guojialing granodiorite (130-126 Ma), and late Cretaceous
128 Aishan granites (118-113 Ma) (Fig. 1a; Yang et al. 2012; Li et al. 2019). Gold
129 deposits in Jiaodong occur as quartz veins and disseminated/stockwork types
130 (Fan et al. 2003). They are mainly hosted by the Linglong and Guojialing
131 granitoids and are strictly controlled by a NNE- to NE- trending fault system
132 (Fig. 1a). Most of these Au deposits have a relatively uniform mineralization
133 age of 126-117 Ma (Cai et al. 2018).

134 The Sanshandao Au deposit, one of the largest disseminated/stockwork
135 type deposit in Jiaodong, has proved Au reserve of >260 t, and recent drill
136 programs have discovered large Au resource at depths (>500t; Wen et al. 2015;
137 Song et al. 2019). The ore bodies are mainly controlled by the NNE- trending
138 and SE-dipping Sanshandao-Cangshang fault, and are mainly enclosed by
139 Archean tonalite-trondhjemite-granodiorite gneisses (Jiaodong group rocks)
140 and Linglong granite in the hanging wall and Guojialing granodiorite in the foot
141 wall (Figs. 1b and 1c; Fan et al. 2003; Wen et al. 2016). The deposit is
142 characterized by extensive hydrothermal alterations that extend ~6 km
143 subvertically along the main fault, with Au ore bodies occurring in the footwall
144 proximally to the fault. The drill holes show that K-feldspar alteration occurs
145 distal to mineralization. This converts into sericitization (\pm silicification), and
146 then, into beresitization proximal to the fault and marks the initiation of Au
147 mineralization (Figs. 1c and 1d). The intensity and width of the alteration
148 generally decreases with increasing depth along the fault, except for K-feldspar

149 alteration that maintains at largely stable thickness (Fig. 1c). The mineralogical
150 and chemical evolution of the hydrothermal alteration are described in detail by
151 Li et al. (2013).

152

153 **PYRITE AND VISIBLE GOLD GENERATIONS**

154 Gold mineralization at Sanshandao occurs as visible Au grains, and shows
155 a close relationship with pyrite and other sulfide minerals. The Au
156 mineralization can be subdivided into three different stages. In this contribution
157 we define “visible Au grains” as individual crystals, generally larger than 1 μm ,
158 which can be observed under optical or scanning electron microscope.

159 Stage 1 beresitization (Fig. 1c) mainly consists of cataclastic quartz (35-
160 45%), feldspar (5-10%), and relatively fine-grained sericite (30-40%) and pyrite
161 (10-20%) (Fig. 2a and 2d). Pyrite in stage 1 (Py1) mainly occurs as euhedral to
162 subhedral, cubic to polygonal grains, ranging in diameter between ca. 10 and
163 1000 μm , and shows close spatial association with sericite (Figs. 3a and 3b).
164 Gold grains occur as small (<1 to 50 μm in diameter) inclusions in Py1 and fill
165 in the grain boundaries of Py1 (Fig. 3a). There is no zonation and chemically
166 heterogeneous texture observed under back-scattered electron (BSE) images for
167 Py1 and the Au grains.

168 Stage 2 is characterized by quartz-pyrite veins. These appear as relatively
169 curved veins in the sericitization, beresitization and K-feldspar zones (Figs. 1d;
170 2b, c, e). The veins consist mainly of quartz (35-55%), pyrite (40-60%) and

171 sericite (5-10%) (Fig. 2e). Pyrite (Py2) occurs as subhedral to anhedral grains
172 with relatively large size up to millimeter level in length (Figs. 3c and 3d).
173 Locally, fractures in Py2 are filled by galena, chalcopyrite, arsenopyrite and
174 sphalerite of stage 3 (Figs. 3e and 3f). Gold grains of stage 2, <1 to 200 μm in
175 size, fill microfractures and boundaries of Py2 grains and occur as inclusions in
176 Py2 (Fig. 3c). Py2 and the Au grains do not exhibit any zonation and chemically
177 heterogeneous texture under BSE images.

178 Stage 3 is marked by quartz-polysulfide veins that develop in the
179 sericitization and beresitization zones, and superposes or crosscuts the quartz-
180 pyrite veins (Figs. 2c and 2f). It mainly consists of quartz (35-50%),
181 polysulfides (50-65%; galena, chalcopyrite, arsenopyrite, pyrite and sphalerite)
182 and sericite (0-5%). Stage 3 pyrite is characterized by a distinct core-rim texture
183 in BSE images, with a dark core (Py3cr) overgrown by a bright euhedral to
184 subhedral rim (Py3; Figs. 3g and 3k). Other sulfide minerals inter-grow and co-
185 precipitate with Py3, and can occur as fine-grained inclusions in Py3cr (Figs.
186 3g and 3k). Gold grains of this stage, varying largely in size (<1 to 500 μm in
187 diameter), co-precipitate with the polysulfides and distribute in contact
188 boundaries between polysulfide and pyrite (Figs. 3e-3j). Sometimes, they occur
189 as inclusions with polysulfide minerals in Py3 (Fig. 7). In addition, some of the
190 Au grains are marked by heterogeneous distribution of Au and Ag, with Ag-rich
191 parts intergrown with Au-rich parts (Figs. 3h-3j). These features distinguish
192 them from the Au grains of earlier stages.

193 Py1 and Py2 can be found at different depths (reaching -3700 m to -4000
194 m), and the early Au mineralization is observed in samples from the
195 underground tunnel, ZK96-3, to ZK96-6 (down to ca. -2650 m; Fig. 1d). The
196 polysulfide assemblages of stage 3 are concentrated at shallow levels, especially
197 for Py3 and arsenopyrite, which are only observed in samples from the
198 underground tunnels (-400 m and -800 m); in the deep area, only limited galena,
199 chalcopyrite and sphalerite are developed. The late Au mineralization is also
200 concentrated in shallow levels, with the deepest example observed at -1447.8 to
201 -1449.8 m (samples of ZK96-3-53 and -54; Fig. 1d), in which argentite is co-
202 precipitated with galena, chalcopyrite and Au grains (Fig. 3l).

203

204 **SAMPLING AND ANALYTICAL METHODS**

205 **Sampling strategy**

206 Representative ore samples were collected from surface to the depth of ca.
207 -4km along the fault from underground tunnels and three drill cores (Figs. 1c
208 and 1d). Samples of beresitization and quartz-pyrite veins were collected from
209 -420 and -800 m depth and drill holes ZK96-3 (-1813 to -2025 m), ZK96-6 (-
210 2516 to -2679 m) and ZK96-5 (-3437 and -3982 m; Fig. 1d). Samples of quartz-
211 polysulfide veins were mainly found and collected from the underground
212 tunnels (-420 and -800 m) and several samples from the drill hole ZK96-3 (-
213 1447.8 to -1449.8 m; -1813 m; Fig. 1d).

214 **Scanning electron microscope (SEM) imaging**

215 Petrographic observation of sulfides and Au minerals were carried out
216 using a Nova NanoSEM 450 field emission SEM at the Institute of Geology and
217 Geophysics, Chinese Academy of Sciences (IGGCAS). Back-scattered electron
218 (BSE) images were acquired with an accelerating voltage of 15 kV and a
219 primary beam current of 20 nA. The instrument is equipped with an X-
220 MAXN80 Energy Dispersive X-ray Spectrometer (EDS) detector, which is used
221 for semiquantitative spot analyses and elemental mapping.

222 **Electron microprobe analysis**

223 Quantitative spot analyses of Au grains and pyrite were performed on a
224 JEOL JXA-8100 electron microprobe at IGGCAS, which was operated with 20
225 kV accelerating voltage and a 10 nA beam current with a 1-3 μm spot diameter.
226 Counting time for each element was 20 s on peak and 10 s on background.
227 Calibration standards used were pyrite for S and Fe, chalcopyrite for Cu,
228 sphalerite for Zn, galena for Pb, and alloy or pure metal for As, Co, Ni, Ag and
229 Au. The detection limits for each element were S (111 ppm), Fe (120 ppm), Co
230 (122 ppm), Ni (100 ppm), Cu (165 ppm), Zn (185 ppm), As (381 ppm), Ag (229
231 ppm), Au (506 ppm), and Pb (309 ppm).

232 **LA-ICP-MS trace element analysis and mapping**

233 Spot and mapping analyses of trace elements in pyrite were conducted with
234 an Agilent 7700x ICP-MS equipped with a Coherent Compex-Pro 193 nm ArF
235 excimer laser generator and an ASI RESOLution-LR-S155 laser microprobe
236 equipped at the State Key Laboratory of Ore Deposit Geochemistry, Institute of

237 Geochemistry, Chinese Academy of Sciences. For spot analysis, the laser was
238 set to a pulse frequency of 5 Hz, an energy intensity of 3 J/cm², and a diameter
239 of 26 μm. During ablation, the sample cell was purged with an atmosphere of
240 Ar (900 mL/min), and then, the ablated materials were transported by He (350
241 mL/min). Each spot analysis included an initial acquisition of background for
242 approximately 30 s with laser off, followed by data acquisition of samples for
243 60 s. In the analytical session, a primary standard of STDGL3, a new series of
244 the STDGL2b-2 (Danyushevsky et al. 2011), was used to calibrate the
245 concentrations of chalcophile and siderophile elements. The lithophile elements
246 were calibrated using GSE-1G and GSD-1G. MASS-1 was analyzed to monitor
247 the analytical accuracy. When compared to preferred values, analytical error
248 was predominantly within 10% (Table 1). For every 10 analyses of samples, the
249 STDGL3 was measured at the beginning and end, with two measurements of
250 GSE-1G and GSD-1G and one measurement of MASS-1. ICPDATA CAL was
251 used for data reduction (Liu et al. 2008), and Fe content of EPMA data was used
252 as the internal standard.

253 Trace element mapping of pyrite were performed by parallel lines of
254 ablation, using the same system. The line ablations were carried out using a spot
255 size of 10 μm or 15 μm with a repetition rate of 10 Hz and a rastering speed of
256 7 μm/s. A set of elements (⁵⁶Fe, ⁵⁹Co, ⁶⁰Ni, ⁶⁵Cu, ⁶⁶Zn, ⁷⁵As, ⁷⁷Se, ⁹⁵Mo, ¹⁰⁷Ag,
257 ¹⁰⁹Ag, ¹²¹Sb, ¹²⁵Te, ¹⁹⁷Au, ²⁰⁸Pb, ²⁰⁹Bi) was chosen for analysis. The acquisition
258 time was set to 0.006 s for most elements, and 0.009 s for ¹⁹⁷Au, ¹⁰⁷Ag and ¹⁰⁹Ag.

259 The total sweep time was ~0.3 s. The mapping of sulfides was initiated and also
260 terminated with two line ablations of STDGL3, GSE-1G and GSD-1G, which
261 were used to calibrate the concentrations of trace elements and to monitor the
262 sensitivity drift, which was shown to be negligible.

263 **LA-MC-ICP-MS sulfur isotope analysis**

264 Sulfur isotope analyses of sulfides were carried out by LA-MC-ICP-MS at
265 the State Key Laboratory of Geological processes and Mineral Resources,
266 China University of Geosciences (Wuhan). A Nu Plasma II MC-ICP-MS
267 equipped with a RESOLUTION S-155 193 nm excimer ArF laser ablation system
268 was used. During experiments, the laser was set to a spot size of 33 μm , a
269 repetition rate of 8Hz and an energy density of 3–4 J/cm^2 . The analysis time for
270 each spot was 65 s, comprising a 25 s measurement of background with laser
271 off and a 40 s sample analysis with laser on. Sample-standard bracketing was
272 used to determine the $\delta^{34}\text{S}$ values of the samples throughout the analytical
273 sessions. An in-house pyrite standard (WS-1, natural pyrite from the Wenshan
274 polymetallic skarn deposit in Yunnan Province of South China; Zhu et al. 2016),
275 was used to calibrate the mass bias for S isotopes. The $\delta^{34}\text{S}_{\text{V-CDT}}$ values ($+1.1\text{‰}$
276 $\pm 0.2\text{‰}$) of WS-1 were determined by SIMS at the Institute of Geochemistry,
277 Chinese Academy of Geochemistry, Guangzhou (Zhu et al. 2016). The true
278 sulfur isotope ratio was calculated by correction for instrumental mass bias by
279 linear interpolation between the biases calculated from two neighboring
280 standard analyses. Standards were analyzed before and after a suite of 5 to 8

281 spot analyses. In this study, the external precision was ca. $\pm 0.4\%$ (2SD).

282

283

RESULTS

284 Fineness of visible gold grains

285 The fineness ($1000 \cdot \text{Au}/(\text{Au}+\text{Ag})$, by weight) of Au grains has been
286 calculated based on EPMA results, with the detailed data in Supplemental Table
287 S1. The Au grains associated with Py1 and Py2 (early generation) show a
288 similar range of high fineness (729-961; Table 2). In the samples at depths of -
289 420 and -800 m, Au grains have a range of fineness of 729 to 807 (mean=752;
290 n=11) and 751 to 859 (mean=785; n=10), respectively. For depths from -1855
291 to -1897 m, the fineness range is 795 to 939, with an average of 855 (n=24). For
292 depths between -2613 and -2650 m, the fineness ranges from 826 to 961, with
293 an average of 870 (n=30). Hence, there is a tendency for fineness of early
294 generation Au grains to increase with depth (Fig. 4).

295 The Au grains associated with polysulfide minerals (late generation) show
296 much lower fineness (218-719) compared with the early generation (Table 2;
297 Fig. 4). Gold grains from the depth of -420 m have fineness of 618 to 709 (mean
298 =649; n=8), whereas those from the depth of -800 m range from 549 to 719
299 (mean=654; n=27). In the heterogeneous Au grains, the silver-rich parts have
300 fineness of 218 to 421 (n=6), and the Au -rich parts have fineness of 634 to 696
301 (n=4). The deepest Au grains of the late generation occur at depths between -
302 1447.8 and -1449.8 m and have fineness range from 623 to 693 (mean=670;

303 n=7).

304 **Trace elements of pyrite**

305 Pyrite of the three stages of mineralization have a range in trace metal
306 contents, with Co, Ni and As showing the greatest variability; both Bi and Au
307 content show moderate variability. The base metals Cu, Zn, Sb and Pb, as well
308 as Ag, show similar ranges of content among the different pyrites. Following
309 Gregory et al. (2019), median and median absolute deviation (MAD) values of
310 the contents are utilized for data interpretations. The trace elemental data for
311 pyrites are summarized in Table 3, and full data sets are provided in
312 Supplemental Table S2.

313 **Py1** is characterized by being enriched in Co (median of 46.0 ppm), Ni
314 (19.6 ppm) and Bi (10.2 ppm), and depleted in As (512 ppm) and Au (0.1 ppm;
315 Table 3; Fig. 5a). With depth decreasing from ca. -3700 m to -420 m, the median
316 content of Co decreases from 247 to 2.6 ppm, with Ni decreasing from 618 to
317 2.5 ppm, and As increasing from 7.2 ppm to 864 ppm (Table 3; Figs. 5b-d).

318 **Py2** also has relatively high contents of Co (median of 8.0 ppm), Ni (10.3
319 ppm) and Bi (2.4 ppm) and low contents of As (41.7 ppm) and Au (BDL) (Table
320 3; Fig. 5a). Similar to Py1, with decreasing depth from ca. -3700 m to -420 m,
321 the median content of Co decreases from 1330 to 1.8 ppm, with Ni decreasing
322 from 158 to 0.4 ppm, and As increasing from 3.5 ppm to 40.9 ppm (Table 3;
323 Figs. 5b-d).

324 **Py3 and Py3cr**, which are developed at shallow level (-420 and -800 m),

325 are distinctly depleted in Co, Ni, and Bi compared to Py1 and Py2, with most
326 spot analyses below detection limits (Table 3; Fig. 5a). Compared to other
327 pyrites, Py3 is markedly enriched in As and Au, with median content are 10000
328 ppm and 2.2 ppm, respectively (Table 3; Fig. 5a).

329 Py1, Py2 and Py3cr show similar range of content ratios of Au/As, Au/Ag,
330 Au/Cu and Au/Pb, which vary significantly and span over 3 to 4 orders of
331 magnitude (Figs. 6a-d). By comparison, Py3 shows higher ratios of Au/Ag,
332 Au/Cu and Au/Pb, due to its higher contents of Au (Figs. 6b-d), and has
333 relatively high and consistent ratios of Au/As. For the ratios of Bi/Pb and Co/Ni,
334 Py1 and Py2 show relatively consistent values lying between 10 and 10⁻¹,
335 whereas, Py3cr and Py3 span largely in the ratio of Bi/Pb and cluster for Co/Ni
336 due to low concentrations (Figs. 6e-f).

337 **Trace element mapping**

338 Trace element mapping by LA-ICP-MS were conducted on two grains of
339 Py3, one of which is shown in Fig. 7. The grain has a quite irregular boundaries
340 between core (Py3cr) and rim (Py3), illustrated by the enrichment of As and Au
341 in Py3 (Fig. 7b-c). Additionally, Py3 is slightly depleted in Ag and Cu relative
342 to Py3cr (Figs. 7d-f), due to abundant micro-inclusions of galena and
343 chalcopyrite in Py3cr (Fig. 7a). The other mapped grain shows similar core-rim
344 trace element patterns (Fig. S1; detailed description given in the Supplemental
345 Material S1).

346 **Sulfur isotope composition of sulfides**

347 Grains of Py1 have $\delta^{34}\text{S}$ ranging from 9.9 to 12.7‰, and the values
348 increase slightly with decreasing depth. From -3600m to -420m, the mean $\delta^{34}\text{S}$
349 values increase from 10.5‰ to 11.1‰, 11.4‰ and 11.8‰ (Table 4; Fig. 8).
350 Grains of Py2 have a predominant $\delta^{34}\text{S}$ range of 8.2 to 11.0‰, although several
351 the deepest samples (> 3000 m) are significantly isotopically lighter (1.5 to
352 5.2‰). At a given depth, Py2 shows lower average $\delta^{34}\text{S}$ than Py1 (Table 4; Fig.
353 8).

354 A smaller number of grains of other sulfides (galena, chalcopyrite,
355 sphalerite, arsenopyrite) were analyzed, which yield $\delta^{34}\text{S}$ generally lower than
356 Py1 and Py2 from similar depths and overlapping the values of Py3 and Py3cr
357 (Table 4; Fig. 8). Aside from the low $\delta^{34}\text{S}$ in the deep Py2 grains, sulfides show
358 a general trend of higher $\delta^{34}\text{S}$ at shallower depths. Noticeably, polysulfides from
359 -1448 m depth have much lower $\delta^{34}\text{S}$ than at other depths (Table 4; Fig. 8).

360

361

DISCUSSION

362 **Two generations of visible Au mineralization**

363 The combination of sulfide mineral assemblages and textures, fineness of
364 Au grains, and trace element geochemistry of sulfides is consistent with the
365 presence of two generations of Au mineralization at Sanshandao. The early
366 generation include beresitization (stage 1) and quartz-pyrite vein (stage 2),
367 where visible Au grains only show relationships with pyrite (Py1 and Py2). This
368 Au is characterized by high fineness of 729-961 (mean=837; Table 2; Fig. 4),

369 dominated by native Au (>800; Hough et al. 2009). These Au grains and
370 associated pyrites are all elementally homogeneous without significant internal
371 zoning. The late generation corresponds to quartz-polysulfide veins (stage 3),
372 where visible Au grains are associated with Py3 and polysulfide minerals. It is
373 characterized by low fineness (mostly 549-719), and chemically heterogeneous
374 textures with Ag-rich parts down to 218-421 (Table 2; Fig. 4). In addition, Py3
375 is distinct in occurring as the rim of pyrite grains and showing a core-rim texture.
376 We suggest that the significant differences between the two generations reflect
377 their distinctly different depositional mechanisms and physicochemical
378 background (Morrison et al. 1991; Gammons and Williams-Jones 1995;
379 Pal'yanova 2008).

380 **Trace elemental evolution of pyrite**

381 Py1 and Py2 are both relatively enriched in Co, Ni and Bi, and depleted in
382 As and Au, (Table 3; Fig. 5a). The chemical features and chemically
383 homogeneous textures features are similar to the disseminated pyrite within
384 altered wall rocks (Peterson and Mavrogenes 2014; Yang et al. 2016), and the
385 pyrite formed under non-boiling fluid conditions (Román et al. 2019).
386 Furthermore, Py1 shows close spatial relationships with sericite within the
387 beresitization zone (Fig. 3a), and the pyrite-quartz veins (Py2) develop irregular
388 and curved boundaries within the hydrothermal alteration zones (Figs. 2a, 2b,
389 2e). These features indicate their successive genesis via fluid-rock interaction
390 (sulfidation of wall rock).

391 Py1 and Py2 show concentrations of Co and Ni increasing with depth but
392 As shows a reverse trend (Figs. 5b-d). The solubilities of chloride complexes of
393 Co and Ni in fluids were determined to be strongly positively related to
394 temperature (Migdisov et al. 2011; Liu et al. 2012), and specifically, a decrease
395 of temperature from 300 to 200°C would lead to a decrease in Co solubility by
396 more than two orders of magnitude. The Co and Ni contents of pyrite may not
397 directly correlate with the temperature of environments, evidenced by some
398 high Co and Ni contents in low temperature environments (Gregory et al. 2019),
399 but, in the context of the Sanshandao deposit, the concentration variations are
400 likely linked to change in temperature. With regard to As, Deditius et al. (2014)
401 summarized a statistical equation of As content in pyrite with temperature: C_{As}
402 $= 0.4785 \cdot e^{-0.0143T}$. According to it, the As content variations of Py1 from 240
403 ppm at ca. -3700 m to ca. 1000 ppm at -420 m (using mean contents here)
404 correspond to temperature varying from ca. 500°C to 400°C. Although the
405 estimated temperature is relatively high compared to the homogenization
406 temperature of early fluid (250 to 400°C; Fan et al. 2003; Hu et al. 2013; Wen
407 et al. 2016), a temperature decrease of <100°C is consistent with the variations
408 in Co, Ni, and As with depth.

409 Py3 is characterized by enrichment in Au and As and marked depletion in
410 Co, Ni and Bi (Table 3; Fig. 5a). The elemental mapping illustrates the irregular
411 and sharp boundaries between core (i.e. Py3cr) and rim (i.e. Py3), with As-rich
412 Py3 encroaching into Py3cr (Figs. 7a-c; S1). Py3cr shows overlapping trace

413 element contents and ratios with Py1 and Py2, save for Co, Ni and Bi (Figs.
414 5a, 6). This suggests Py3 is formed by replacement of early pyrite (mainly Py2)
415 via a dissolution-reprecipitation reaction, with the relic of early pyrite as core
416 (Py3cr).

417 The dissolution-reprecipitation reaction is kinetically controlled by the
418 relative solubility of the parent and product phase in fluid (Putnis 2002). For
419 sulfide minerals, the relative solubilities mainly depend on the T, P, pH, f_{O_2} , f_{S_2} ,
420 and ligand concentration of fluid (Hemley et al. 1992; Reed and Palandri 2006;
421 Sung et al. 2009). The sharp textural and compositional boundaries between the
422 core and rim are likely reflective of sudden variations in fluid pressure (Peterson
423 and Mavrogenes 2014). The abundance of sulfide micro-inclusions in Py3 and
424 Py3cr, likely formed by preferential replacement of early pyrite by rapid
425 percolation of fluid along fractures and a pore network (Fig. 7; Voute et al. 2019),
426 is also indicative of rapid ingress of fluid, which can be readily achieved by
427 decompression (Weatherley and Henley 2013). Meanwhile, significant
428 decompression would further cause phase separation of H₂O-CO₂-NaCl fluid
429 (Wilkinson and Johnston 1996; Velásquez et al. 2014), which is shown by the
430 coexistence of CO₂-H₂O and H₂O-NaCl fluid inclusions in sphalerite of stage 3
431 (Hu et al. 2013; Wen et al. 2016). Moreover, decompression would promote
432 higher solubilities of pyrite until fluid enters the two-phase field in temperature-
433 composition space, where the solubilities would eventually decrease (Hemley
434 et al. 1992). Hence, the formation of Py3 was likely controlled by

435 decompression. Additionally, under the phase separation background, As would
436 be enriched in the fluid (Libbey and Williams-Jones 2016; Simmons et al. 2016),
437 which contributed to coupled incorporation of As and Au into Py₃ (Deditius et
438 al. 2014; Kusebauch et al. 2019; Xing et al. 2019) and deposition of arsenopyrite
439 (Pokrovski et al. 2002). Concomitant rapid cooling would lead to depletion of
440 Co, Ni and Bi in fluid (Migdisov et al. 2011; Liu et al. 2012; Tooth et al. 2013)
441 and the abundant deposition of base metal sulfide minerals (e.g. galena,
442 chalcopyrite and sphalerite). The corresponding chemical features further
443 indicate that Py₃ and polysulfides are generated under significant
444 decompression and resultant phase separation of fluid.

445 The significant decompression may be related to activities of secondary
446 faults and expansion of new fractures (Xinli Au deposit, ca. 4km southwest to
447 Sanshandao along Cangshang-Sanshandao fault; Yang et al. 2018). In contrast
448 to the distribution of stage 1 and 2 at variable depths, stage 3 mineralization is
449 concentrated on upper areas (<-1500 m depth). The difference in spatial
450 distribution may relate to the more brittle behavior of rocks in the shallowest
451 part of the deposit.

452 **Sulfur isotopic evolution of pyrite and polysulfides**

453 Sulfur isotopes in pyrite and polysulfides at Sanshandao vary temporally
454 and spatially, reflecting a variation in physicochemical conditions as fluids
455 migrated upward. The source of sulfur is not the focus in the present study and
456 will not be discussed here, rather we will focus on the reasons for the isotopic

457 variation with depth.

458 The $\delta^{34}\text{S}$ values of Py1 (9.9 to 12.7‰; Table 4) is higher than Py2, of which
459 most range from 8.2 to 11.0‰, with a minority of samples between 1.5 and 5.2‰
460 (Table 4; Fig. 8). However, the $\delta^{34}\text{S}$ difference may not be explained by
461 deposition of Py1 leading to lower sulfur isotopes of remaining fluid, according
462 to the -1.9‰ equilibrium $^{34}\text{S}/^{32}\text{S}$ fractionation between pyrite and H_2S in
463 Syverson et al. (2015). The $\delta^{34}\text{S}$ values of Py1 are similar to the pyrite of
464 disseminated-type deposits at Jiaodong (typically 9 to 12‰; Mao et al. 2008;
465 Zhu et al. 2018), where sulfidation is the dominant Au and sulfide deposition
466 mechanism. Py1 was generated after extensive fluid-rock interactions (i.e. K-
467 feldspar alteration, sericitization and silicification), and from which CH_4 was
468 derived (Fan et al. 2003; Wen et al. 2016), indicating a decrease of f_{O_2} (Li et al.
469 2013). Hence, the parental fluid should correspond to lower $\delta^{34}\text{S}$ values in
470 pyrite than those in Py1, since reduction would cause an increase of $\delta^{34}\text{S}$ value
471 (Ohmoto 1972; Seal 2006). Quartz-pyrite (Py2) veins were emplaced in more
472 interconnected spaces, and the sulfur isotopes of the fluid were less influenced
473 by reduction, leading to lower $\delta^{34}\text{S}$ values in Py2 than in Py1.

474 Spatially, from ca. -3900 to -420 m, the $\delta^{34}\text{S}$ values of Py1 increase
475 successively from 10.5‰ to 11.8‰, while, Py2 maintain at ca. 10.0‰ (Table 4;
476 Fig. 8). The $\delta^{34}\text{S}$ increase is likely related to elevated degree of fluid-rock
477 interaction, indicated by the more extensive hydrothermal alteration at
478 relatively shallow depths (Figs. 1c and 1d; Fig. 9).

479 Low $\delta^{34}\text{S}$ values of Py2 (1.5 to 5.2‰) were obtained from several samples
480 in hole ZK96-5 (-3437 and -3581 m depth), in rock with weak hydrothermal
481 alterations (Figs. 1c and 1d). Wen et al. (2016) also obtained low $\delta^{34}\text{S}$ values
482 ranging from 1.9 to 3.5‰ in bulk pyrite collected in weak K-feldspar alteration
483 zone and Jiaodong group away from the main fault. Based on these observations,
484 we suggest that the low $\delta^{34}\text{S}$ may derive from Precambrian basement rocks (-
485 1.3 to 7.8‰; Wang et al. 2002).

486 The $\delta^{34}\text{S}$ values of polysulfides in stage 3 do not vary significantly with
487 depths, but show noticeably lower values at hole ZK96-3 (-1448 to -1909 m
488 depth; Table 4; Fig. 8). As discussed above, we interpret the deposition of
489 polysulfides in the shallow portion of the deposit to have been triggered by
490 decompression and phase separation of fluid, which led to sharp decrease of
491 $\delta^{34}\text{S}$ values of hydrothermal minerals due to rapid loss of reduced gases (e.g.
492 H_2 , CH_4 , H_2S) and the resultant increase in the ratio of S^{6+}/S^2 in residual fluid
493 (Drummond and Ohmoto 1985; Mckibben and Eldridge 1990). Noticeably, the
494 samples with the lowest $\delta^{34}\text{S}$ (ZK96-3-53 and -54) contain the observed deepest
495 Au mineralization of the late generation, with co-deposition of argentite (Fig.
496 3l). Hence, we deduce that the pressure drop and phase separation of fluid might
497 commence at the current depth of ca. -1500 m, supported by the large variation
498 in fluid inclusion salinity between -1373 and -1666 m depth (Wen et al. 2016).
499 In the shallower portion of the deposit, the $\delta^{34}\text{S}$ values of Py3 and polysulfides
500 rise again, which was likely related to the deposition of galena and chalcopyrite

501 (Ohmoto 1972; Seal 2006).

502 **Controls on deposition of visible Au grains and fineness variation**

503 The high fineness (729-961) of early Au generation is similar to orogenic
504 and Carlin-type Au deposits (typically 750-1000 in Morrison et al. 1991), where
505 sulfidation of wall rock is the major mineralizing mechanism (Large et al. 2011;
506 Kusebauch et al. 2019), consistent with Py1 and Py2 (Fig. 9). Consistent with
507 the CO₂-H₂O-CH₄ fluid (Fan et al. 2003; Hu et al. 2013; Wen et al. 2016) and
508 physicochemical conditions (weakly acidic and reducing) of stage 1 and 2, Au
509 is transported as sulfur complexes (Au(HS)⁰/Au(HS)₂⁻), and Ag as chloride
510 complexes (AgCl₂⁻) at Sanshandao (Morrison et al. 1991; William-Jones et al.
511 2009; Pal'yanova 2008). Desulfidation of fluid for depositing Py1 and Py2
512 would destroy Au-S complexes, but have limited influence on Ag-Cl complexes,
513 contributing to high fineness of Au grains (Morrison et al. 1991). Meanwhile,
514 the production of CH₄ and decrease of *f*_{O₂} further promotes the saturation and
515 deposition of Au (Williams-Jones et al. 2009; Kusebauch et al. 2019). Likewise,
516 the As(OH)₃⁰ (Pokrovski et al. 2002; Kusebauch et al. 2019) and Cl⁻ complexes
517 of Cu, Pb and Zn (Reed and Palandri 2006) would not be significantly affected,
518 and were transported to shallow depths (Fig. 9). The markedly different fate of
519 Au with other metals in the process also accounts for the 3 to 4 order of
520 magnitude variation of Au/As, Au/Ag, Au/Cu and Au/Pb in Py1 and Py2
521 (Kusebauch et al. 2019; Fig. 6).

522 Noticeably, fineness of the early Au grains decreases from 870 to 752 with

523 decreasing depth from -2650 m to -420 m (Table 2; Figs. 4 and 9). The fineness
524 variation is a complex function of multiple physicochemical parameters (e.g.,
525 temperature, f_{S_2} , f_{O_2} , Cl^- concentration, pH and $\sum Au/Ag$) of fluid (Gammons
526 and Williams-Jones 1995; Pal'yanova 2008). The stabilization of pyrite and
527 sericite, and the saturation of Au at different depths suggest that no obvious
528 change of f_{S_2} , f_{O_2} , pH and $\sum Au/Ag$ of fluid has occurred. Hence, the decrease of
529 Au fineness is likely attributed to a decrease of temperature (Fig. 9), since
530 temperature is positively correlated with fineness (Gammons and Williams-
531 Jones 1995; Pal'yanova 2008). Temperature decrease is also consistent with
532 trace element variations in Py1 and Py2 with depth (i.e. Co, Ni and As).
533 Although homogenization temperatures of fluid inclusions have found no
534 obvious variation -4000 m to surface (Wen et al. 2016), the trapping
535 temperatures corrected by pressure variations (ca. 110 MPa lithostatic pressure)
536 correspond to a decrease of $<100^\circ C$, consistent with the estimate based on As
537 in Py1. Meanwhile, the enhanced degree of fluid-rock interaction, indicated by
538 more extensive hydrothermal alterations (Fig. 9), was accompanied with
539 increased reduction of the fluid, as evidenced by the presence of CH_4 in fluid
540 inclusion from depth shallower than -3000 m (Wen et al. 2016). This is
541 consistent with the initiation of visible Au mineralization at ca. -2700 m. Hence,
542 from a spatial perspective, successive cooling (+decompression) and enhanced
543 fluid-rock interaction controlled the deposition of Au grains and the variation
544 of fineness (Fig. 9).

545 The late Au mineralization is marked by distinctly lower fineness (mostly
546 549-719 down to 218-421), similar to epithermal deposits (typically 440-1000
547 in Morrison et al. 1991). A pressure drop and phase separation of late
548 mineralizing fluids would effectively destabilize Au-S and Ag-Cl complexes at
549 the same time (Seward 1976; Morrison et al. 1991; Pal'yanova 2008; Williams-
550 Jones et al. 2009), contributing to low fineness of visible Au grains (Fig. 9). In
551 addition, the subsequent rapid cooling would drive more intense dissociation of
552 Ag-Cl complexes and deposit Ag-rich grains (218-421 fineness). The lower
553 fineness grains would be intimately intergrown with grains of higher fineness
554 precipitated slightly earlier, leading to the chemical heterogeneity displayed by
555 late Au mineralization. In the intense process, most ore elements in the fluid
556 (e.g. As, Cu, Pb, Zn) were destabilized and saturated to deposit polysulfide
557 minerals (Fig. 9). The coupled behavior of the elements in the process ensured
558 Au incorporation with As to form invisible Au, which is also demonstrated by
559 the consistent Au/As in Py3 (Fig. 6a; Kusebauch et al. 2019). From a spatial
560 perspective, this ore-forming process focused on the shallow area in the deposit
561 (Fig. 9).

562 **Remobilization to form visible gold mineralization?**

563 It has been commonly established that remobilization or redistribution of
564 invisible Au in sulfides may result in formation of visible Au in orogenic Au
565 deposits (Morey et al. 2008; Large et al. 2009, 2011; Sung et al. 2009; Cook et
566 al. 2013; Fougrouse et al. 2016; Gregory et al. 2016; Cromie et al. 2018; and

567 references therein). In the present study, Au mineralization is dominant by
568 visible Au grains, except for the arsenian Py3 with a relatively high content of
569 Au. In addition to enrichment in As and Au, mobilization of trace elements
570 during dissolution reprecipitation reactions is also apparent in Py3 by depletion
571 of Co, Ni and Bi. However, it does not favor remobilization of Au to form
572 visible Au for following reasons. First, Py1 and Py2 have low concentration of
573 Au (Fig. 5a), with major analytical spots below detection limits, even if 100%
574 of the Au in Py1 and Py2 was remobilized, the mass of Au could not match the
575 large tonnage of the deposit (Yang et al. 2016). Second, Au mineralization in
576 early pyrite generations is also predominantly by visible Au, distributed in
577 fractures and grain boundaries of Py1 and Py2. The early pyrite generations do
578 not show any evidence of chemical remobilization (Figs. 3b and 3d). Finally,
579 visible Au of the late generation is significantly Ag-rich, in contrast to what
580 would be expected from remobilization (Zoheir et al. 2008; Liu et al. 2018; Li
581 et al. 2019), likely due to higher solubility and mobility of silver (Morrison et
582 al. 1991).

583

584

IMPLICATIONS

585 In this contribution, two generations of Au mineralization have been
586 recognized at Sanshandao. The early Au mineralization is characterized by Au
587 grains with high fineness. In contrast, late mineralization is distinct, with a
588 polysulfide mineral association and Au grains with low fineness. The two

589 generations of Au mineralization are attributed to sulfidation of wallrocks, and
590 decompression and phase separation of the fluid, respectively. The two
591 mechanisms are likely dominant in the disseminated-type deposits and quartz
592 vein-type deposits, respectively, which is observed in the Au deposits at
593 Jiaodong (e.g. Fan et al. 2003; Yang et al. 2016; Feng et al. 2018; Li et al.
594 2018). This study suggests that the two distinct drivers for mineralization can
595 act in one single deposit.

596 In this research, we relate the textural and chemical features of the pyrites
597 to their depositional mechanisms. The pyrite (Py1 and Py2) formed under
598 sulfidation process of wallrocks is characterized by chemically homogeneous
599 texture, with relatively high concentrations of Co and Ni and low concentrations
600 of As and Au. These pyrites are similar to pyrite of orogenic Au deposits
601 (Gregory et al. 2019), formed through sulfidation processes. In contrast, Py3
602 formed from phase separation of fluid (decompression). This generation occurs
603 as the rim of pyrite grains and is characterized by relatively high concentrations
604 of As and Au and low concentrations of Co and Ni. The abundant co-deposition
605 of low fineness Au, chalcopyrite and galena show the simultaneous significant
606 instabilities of Ag, Cu and Pb in the fluid. By comparison, the two different
607 pyrites are analogous to the pyrites formed under non-boiling and boiling fluids
608 as summarized by Román et al. (2019). As fluid conditions change, the behavior
609 of Co and Ni are generally the reverse of that exhibited by As, Ag, Au, as well
610 as Cu, Zn, Pb, and Sb, as recorded by pyrite (Peterson and Mavrogenes 2014;

611 Román et al. 2019). In brief, we stress that the linking between the textural and
612 chemical features of pyrite to the depositional mechanism can be applied
613 universally.

614 Trace elements and sulfur isotopes in sulfides have been explored in
615 numerous studies of different deposits (e.g. Peterson and Mavrogenes 2014;
616 Steadman et al. 2015; Gregory et al. 2016; LaFlamme et al. 2018; Voute et al.
617 2019), whereas, few studies have focused on the evolution with depth and
618 integrated these with the spatial variation of Au fineness. In this research, Co,
619 Ni and As concentrations of pyrite, sulfur isotopes and Au fineness changed
620 gradually with depth or temperature under steady fluid conditions (single-phase)
621 during early mineralization. When the fluid system changed suddenly into a
622 two-phase condition, the result was distinct depletion of Co and Ni and
623 enrichment of As in pyrite (Tardani et al. 2017; Román et al. 2019), and abrupt
624 decrease in $\delta^{34}\text{S}$ and Au fineness (Mckibben and Eldridge 1990; Morrison et al.
625 1991). Hence, the spatial variations of these elements and sulfur isotopes can
626 also provide critical information for the physicochemical conditions and
627 evolution of fluid system.

628

629

ACKNOWLEDGMENTS

630 We thank Xin Yan, Di Zhang, Ting-Guang Lan, Zhi-Hui Dai and Kui-Dong
631 Zhao for their help in SEM, EMP, LA-ICP-MS and LA-MC-ICP-MS analyses.

632 Xiao-Hui Jiang are thanked for her help on sampling. We are grateful to Daniel

633 Gregory and an anonymous referee for their constructive feedback that helped
634 to improve an earlier draft of the manuscript, and associate editor Paul
635 Tomascak for valuable suggestions and efficient editorial handling. This study
636 was financially supported by the National Key Research and Development
637 Program (No. 2016YFC0600105) and National Natural Science Foundation of
638 China (41672094).

639

REFERENCES CITED

640

641 Benning, L.G., Seward, T. M. (1996) Hydrosulphide complexing of Au (I) in
642 hydrothermal solutions from 150–400 °C and 500–1500 bar. *Geochimica*
643 *et Cosmochimica Acta*, 60, 1849-1871.

644 Cai, Y.C., Fan, H.R., Santosh, M., Hu, F.F., Yang, K.F., Li, X.H. (2018)
645 Decratonic gold mineralization: evidence from the Shangzhuang gold
646 deposit, eastern North China Craton. *Gondwana Research*, 54, 1-22.

647 Cook, N.J., Ciobanu, C.L., Meria, D., Silcock, D., Wade, B. (2013)
648 Arsenopyrite-pyrite association in an orogenic gold ore: Tracing
649 mineralization history from textures and trace elements. *Economic*
650 *Geology*, 108, 1273-1283.

651 Cromie, P., Makoundi, C., Zaw, K., Cooke, D.R., White, N., Ryan, C. (2018)
652 Geochemistry of Au-bearing pyrite from the Sepon Mineral District, Laos
653 DPR, Southeast Asia: Implications for ore genesis. *Journal of Asian Earth*
654 *Sciences*, 164, 194-218.

655 Danyushevsky, L., Robinson, P., Gilbert, S., Norman, M., Large, R.,
656 McGoldrick, P., Shelley, M. (2011) Routine quantitative multi-element
657 analysis of sulphide minerals by laser ablation ICP-MS: Standard
658 development and consideration of matrix effects. *Geochemistry-*
659 *Exploration Environment Analysis*, 11, 51-60.

660 Deditius, A.P., Reich, M., Kesler, S.E., Utsunomiya, S., Chryssoulis, S.L.,
661 Walshe, J., Ewing, R.C. (2014) The coupled geochemistry of Au and As in

- 662 pyrite from hydrothermal ore deposits. *Geochimica et Cosmochimica Acta*,
663 140, 644-670.
- 664 Drummond, S.E., Ohmoto, H. (1985) Chemical evolution and mineral
665 deposition in boiling hydrothermal systems. *Economic Geology*, 80, 126-
666 147.
- 667 Fan, H.R., Zhai, M.G., Xie, Y.H., Yang, J.H. (2003) Ore-forming fluids
668 associated with granite hosted goldmineralization at the Sanshandao
669 deposit, Jiaodong gold province, China. *Mineralium Deposita*, 38, 739-750.
- 670 Feng, K., Fan, H.R., Hu, F.F., Yang, K.F., Liu, X., Shangguan, Y.N., Cai, Y.C.,
671 Jiang, P. (2018) Involvement of anomalously As-Au-rich fluids in the
672 mineralization of the Heilan'gou gold deposit, Jiaodong, China: Evidence
673 from trace element mapping and in-situ sulfur isotope composition.
674 *Journal of Asian Earth Sciences*, 160, 304-321.
- 675 Fougereuse, D., Micklethwaite, S., Tomkins, A.G., Mei, Y., Kilburn, M.,
676 Guagliardo, P., Fisher, L.A., Halfpenny, A., Gee, M., Paterson, D., Howard,
677 D.L. (2016) Gold remobilisation and formation of high grade ore shoots
678 driven by dissolution-reprecipitation replacement and Ni substitution into
679 auriferous arsenopyrite. *Geochimica et Cosmochimica Acta*, 178, 143-159.
- 680 Gammons, C.H., Williams-Jones, A.E. (1995) Hydrothermal geochemistry of
681 electrum: thermodynamic constraints. *Economic Geology*, 90, 420-432.
- 682 Gregory, D.D., Large, R.R., Bath, A.B., Steadman, J.A., Wu, S., Danyushevsky,
683 L., Bull, S. W., Holden P., Ireland T. R. (2016) Trace element content of

- 684 pyrite from the Kapaï Slate, St. Ives gold district, Western Australia.
685 Economic Geology, 111, 1297-1320.
- 686 Gregory, D.D., Cracknell, M.J., Large, R.R., McGoldrick, P., Kuhn, S.,
687 Maslennikov, V.V., Baker, M.J., Ivan Belousov, N.F., Figueroa M.C.,
688 Steadman, J.A., Fabris, A.J., Lyons, T.W. (2019) Distinguishing ore
689 deposit type and barren sedimentary pyrite using laser ablation-inductively
690 coupled plasma-mass spectrometry trace element data and statistical
691 analysis of large data sets. Economic Geology 114, 771-786.
- 692 Hemley, J.J., Cygan, G.L., Fein, J.B., Robinson, G.R., D'Angelo, W.M. (1992)
693 Hydrothermal ore-forming processes in the light of studies in rock-
694 buffered systems; I, Iron-copper-zinc-lead sulfide solubility relations.
695 Economic Geology, 87, 1-22.
- 696 Hough, R.M., Butt, C.R., Fischer-Bühner, J. (2009) The crystallography,
697 metallography and composition of gold. Elements, 5, 297-302.
- 698 Hu, F.F., Fan, H.R., Jiang, X.H., Li, X.C., Yang, K.F., Mernagh, T. (2013) Fluid
699 inclusions at different depths in the Sanshandao gold deposit, Jiaodong
700 Peninsula, China. Geofluids, 13, 528-541.
- 701 Kusebauch, C., Gleeson, S.A., Oelze, M. (2019) Coupled partitioning of Au and
702 As into pyrite controls formation of giant Au deposits. Science advances,
703 5, eaav5891.
- 704 LaFlamme, C., Sugiono, D., Thébaud, N., Caruso, S., Fiorentini, M., Selvaraja,
705 V., Jeon, H., Voute, F., Martin L. (2018) Multiple sulfur isotopes monitor

- 706 fluid evolution of an Archean orogenic gold deposit. *Geochimica et*
707 *Cosmochimica Acta*, 222, 436-446.
- 708 Large, R.R., Danyushevsky, L., Hollit, C., Maslennikov, V., Meffre, S., Gilbert,
709 S., Bull, S., Scott, R., Embsbo, P., Thomas, H., Singh, B., Foster, J. (2009)
710 Gold and trace element zonation in pyrite using a laser imaging technique:
711 Implications for the timing of gold in orogenic and Carlin-style sediment-
712 hosted deposits. *Economic Geology*, 104, 635-668.
- 713 Large, R.R., Bull, S.W., Maslennikov, V.V. (2011) A carbonaceous sedimentary
714 source-rock model for Carlin-type and orogenic gold deposits. *Economic*
715 *Geology*, 106, 331-358.
- 716 Li, W., Cook, N.J., Ciobanu, C.L., Xie, G., Wade, B.P., Gilbert, S.E. (2019)
717 Trace element distributions in (Cu)-Pb-Sb sulfosalts from the Gutaishan
718 Au-Sb deposit, South China: Implications for formation of high fineness
719 native gold. *American Mineralogist*, 104, 425-437.
- 720 Li, X.C., Fan, H.R., Santosh, M., Hu, F.F., Yang, K.F., Lan, T.G. (2013)
721 Hydrothermal alteration associated with Mesozoic granite-hosted gold
722 mineralization at the Sanshandao deposit, Jiaodong gold province, China.
723 *Ore Geology Reviews*, 53, 403-421.
- 724 Li, X.H., Fan, H.R., Yang, K.F., Hollings, P., Liu, X., Hu, F.F., Cai, Y.C. (2018)
725 Pyrite textures and compositions from the Zhuangzi Au deposit,
726 southeastern North China Craton: implication for ore-forming processes.
727 *Contributions to Mineralogy and Petrology*, 173, 73.

- 728 Li, X.H., Fan, H.R., Hu, F.F., Hollings, P., Yang, K.F., Liu, X. (2019) Linking
729 lithospheric thinning and magmatic evolution of late Jurassic to early
730 Cretaceous granitoids in the Jiaobei Terrane, southeastern North China
731 Craton. *Lithos*, 324, 280-296.
- 732 Liang, Y., Hoshino, K. (2015) Thermodynamic calculations of Au_xAg_{1-x} -Fluid
733 equilibria and their applications for ore-forming conditions. *Applied*
734 *Geochemistry*, 52, 109-117.
- 735 Libbey, R.B., Williams-Jones, A.E. (2016) Relating sulfide mineral zonation
736 and trace element chemistry to subsurface processes in the Reykjanes
737 geothermal system, Iceland. *Journal of Volcanology and Geothermal*
738 *Research*, 310, 225-241.
- 739 Liu, A.L., Jiang, M.R., Ulrich, T., Zhang, J., Zhang, X.J. (2018) Ore genesis of
740 the Bake gold deposit, southeastern Guizhou province, China: Constraints
741 from mineralogy, in-situ trace element and sulfur isotope analysis of pyrite.
742 *Ore Geology Reviews*, 102, 740-756.
- 743 Liu, W., Migdisov, A., Williams-Jones, A. (2012) The stability of aqueous
744 nickel (II) chloride complexes in hydrothermal solutions: Results of UV-
745 Visible spectroscopic experiments. *Geochimica et Cosmochimica Acta*, 94,
746 276-290.
- 747 Liu, Y., Hu, Z., Gao, S., Xu, J., Gao, C., Chen, H. (2008) In situ analysis of
748 major and trace elements of anhydrous minerals by LA-ICP-MS without
749 applying an internal standard. *Chemical Geology*, 257, 34-43.

- 750 Mao, J.W., Wang, Y.T., Li, H.M., Pirajno, F., Zhang, C.Q., Wang, R.T. (2008)
751 The relationship of mantle-derived fluids to gold metallogenesis in the
752 Jiaodong Peninsula: evidence from D–O–C–S isotope systematics. *Ore*
753 *Geology Reviews*, 33, 361-381.
- 754 McKibben, M.A., Eldridge, C.S. (1990) Radical sulfur isotope zonation of
755 pyrite accompanying boiling and epithermal gold deposition: a SHRIMP
756 study of the Valles Caldera, New Mexico. *Economic Geology*, 85, 1917-
757 1925.
- 758 Migdisov, A.A., Zezin, D., Williams-Jones, A.E. (2011) An experimental study
759 of cobalt (II) complexation in Cl⁻ and H₂S-bearing hydrothermal solutions.
760 *Geochimica et Cosmochimica Acta*, 75, 4065-4079.
- 761 Morey, A.A., Tomkins, A.G., Bierlein, F.P., Weinberg, R.F., Davidson, G.J.
762 (2008) Bimodal distribution of gold in pyrite and arsenopyrite: examples
763 from the Archean Boorara and Bardoc shear systems, Yilgarn Craton,
764 Western Australia. *Economic Geology*, 103, 599-614.
- 765 Morrison, G.W., Rose, W.J., Jaireth, S. (1991) Geological and geochemical
766 controls on the silver content (fineness) of gold in gold-silver deposits. *Ore*
767 *Geology Reviews*, 6, 333-364.
- 768 Ohmoto, H. (1972) Systematics of sulfur and carbon isotopes in hydrothermal
769 ore deposits. *Economic Geology*, 67, 551-578.
- 770 Pal'yanova, G. (2008) Physicochemical modeling of the coupled behavior of
771 gold and silver in hydrothermal processes: Gold fineness, Au/Ag ratios and

- 772 their possible implications. *Chemical Geology*, 255, 399-413.
- 773 Peterson, E.C., Mavrogenes, J.A. (2014) Linking high-grade gold
774 mineralization to earthquake-induced fault-valve processes in the Porgera
775 gold deposit, Papua New Guinea. *Geology*, 42, 383-386.
- 776 Pokrovski, G.S., Kara, S., Roux, J. (2002) Stability and solubility of
777 arsenopyrite, FeAsS, in crustal fluids. *Geochimica et Cosmochimica Acta*,
778 66, 2361-2378.
- 779 Putnis, A. (2002) Mineral replacement reactions: from macroscopic
780 observations to microscopic mechanisms. *Mineralogical Magazine*, 66,
781 689-708.
- 782 Reed, M.H., Palandri, J. (2006) Sulfide mineral precipitation from
783 hydrothermal fluids. *Reviews in Mineralogy and Geochemistry*, 61(1),
784 609-631.
- 785 Román, N., Reich, M., Leisen, M., Morata, D., Barra, F., Deditius, A.P. (2019)
786 Geochemical and micro-textural fingerprints of boiling in pyrite.
787 *Geochimica et Cosmochimica Acta*, 246, 60-85.
- 788 Seal, R.R. (2006) Sulfur isotope geochemistry of sulfide minerals. *Reviews in*
789 *Mineralogy and Geochemistry*, 61(1), 633-677.
- 790 Seward, T.M. (1976) The stability of chloride complexes of silver in
791 hydrothermal solutions up to 350 °C. *Geochimica et Cosmochimica Acta*,
792 40, 1329-1341.
- 793 Simmons, S.F., Brown, K.L., Tutolo, B.M. (2016) Hydrothermal transport of

- 794 Ag, Au, Cu, Pb, Te, Zn, and other metals and metalloids in New Zealand
795 geothermal systems: Spatial patterns, fluid-mineral equilibria, and
796 implications for epithermal mineralization. *Economic Geology*, 111, 589-
797 618.
- 798 Song, M.C., Song, Y.X., Ding, Z.J., Wei, X.F., Sun, S.L., Song, G.Z., Zhang,
799 J.J., Zhang, P.J., Wang, Y.G. (2019) The discovery of the Jiaojia and the
800 Sanshandao giant gold deposits in Jiaodong Peninsula and discussion on
801 the relevant issues. *Geotectonica et Metallogenia*, 43, 92-110 (in Chinese
802 with English abstract).
- 803 Steadman, J.A., Large, R.R., Meffre, S., Olin, P.H., Danyushevsky, L.V.,
804 Gregory, D.D., Belousov, I., Lounejeva, E., Ireland, T.R., Holden, P. (2015)
805 Synsedimentary to early diagenetic gold in black shale hosted pyrite
806 nodules at the Golden Mile deposit, Kalgoorlie, Western Australia.
807 *Economic Geology*, 110, 1157-1191.
- 808 Stefánsson, A., Seward, T.M. (2003) Experimental determination of the stability
809 and stoichiometry of sulphide complexes of silver (I) in hydrothermal
810 solutions to 400 °C. *Geochimica et Cosmochimica Acta*, 67, 1395-1413.
- 811 Sung, Y.H., Brugger, J., Ciobanu, C.L., Pring, A., Skinner, W., Nugus, M. (2009)
812 Invisible gold in arsenian pyrite and arsenopyrite from a multistage
813 Archaean gold deposit: Sunrise Dam, Eastern Goldfields Province,
814 Western Australia. *Mineralium Deposita*, 44, 765-791.
- 815 Syverson, D.D., Ono, S., Shanks, W.C., Seyfried Jr, W.E. (2015) Multiple sulfur

- 816 isotope fractionation and mass transfer processes during pyrite
817 precipitation and recrystallization: an experimental study at 300 and
818 350 °C. *Geochimica et Cosmochimica Acta*, 165, 418-434.
- 819 Tardani, D., Reich, M., Deditius, A.P., Chryssoulis, S., Sánchez-Alfaro, P.,
820 Wrage J., Roberts M.P. (2017) Copper-arsenic decoupling in an active
821 geothermal system: a link between pyrite and fluid composition.
822 *Geochimica et Cosmochimica Acta*, 204, 179-204.
- 823 Tooth, B., Etschmann, B., Pokrovski, G.S., Testemale, D., Hazemann, J.L.,
824 Grundler, P.V., Brugger, J. (2013) Bismuth speciation in hydrothermal
825 fluids: An X-ray absorption spectroscopy and solubility study. *Geochimica*
826 *et Cosmochimica Acta*, 101, 156-172.
- 827 Velásquez, G., Béziat, D., Salvi, S., Siebenaller, L., Borisova, A.Y., Pokrovski,
828 G.S., De Parseval, P. (2014) Formation and deformation of pyrite and
829 implications for gold mineralization in the El Callao District, Venezuela.
830 *Economic Geology*, 109, 457-486.
- 831 Voute, F., Hagemann, S.G., Evans, N.J., Villanes, C. (2019) Sulfur isotopes,
832 trace element, and textural analyses of pyrite, arsenopyrite and base metal
833 sulfides associated with gold mineralization in the Pataz-Parcoy district,
834 Peru: implication for paragenesis, fluid source, and gold deposition
835 mechanisms. *Mineralium Deposita*, 54, 1077-1100.
- 836 Wang, Y.W., Zhu, F.S., Gong, R.T. (2002) Tectonic isotope geochemistry–
837 further study on sulphur isotope of Jiaodong Gold Concentration Area.

- 838 Gold, 23, 1-16 (in Chinese with English abstract).
- 839 Weatherley, D.K., Henley, R.W. (2013) Flash vaporization during earthquakes
840 evidenced by gold deposits. *Nature Geoscience*, 6, 294-298.
- 841 Wen, B.J. (2015) Fluid evolution and ore genesis of typical gold deposits in the
842 Northwest Jiaodong, Southeastern North China Craton: Unpublished Ph.D.
843 thesis, Beijing, China, The University of Chinese Academy of Sciences,
844 164p (in Chinese with English abstract).
- 845 Wen, B.J., Fan, H.R., Hu, F.F., Liu, X., Yang, K.F., Sun, Z.F., Sun, Z.F. (2016)
846 Fluid evolution and ore genesis of the giant Sanshandao gold deposit,
847 Jiaodong gold province, China: constraints from geology, fluid inclusions
848 and H–O–S–He–Ar isotopic compositions. *Journal of Geochemical
849 Exploration*, 171, 96-112.
- 850 Wilkinson, J.J., Johnston, J.D. (1996) Pressure fluctuations, phase separation,
851 and gold precipitation during seismic fracture propagation. *Geology*, 24,
852 395-398.
- 853 Williams-Jones, A.E., Bowell, R.J., Migdisov, A.A. (2009) Gold in solution.
854 *Elements*, 5, 281-287.
- 855 Wilson, S.A., Ridley, W.I., Koenig, A.E. (2002) Development of sulfide
856 calibration standards for the laser ablation inductively-coupled plasma
857 mass spectrometry technique. *Journal of Analytical Atomic Spectroscopy*,
858 17, 406-409.
- 859 Xing, Y., Brugger, J., Tomkins, A., Shvarov, Y. (2019) Arsenic evolution as a

- 860 tool for understanding formation of pyritic gold ores. *Geology*, 47, 335-
861 338.
- 862 Yang, K.F., Fan, H.R., Santosh, M., Hu, F.F., Wilde, S.A., Lan, T.G., Liu, Y.S.
863 (2012) Reactivation of the Archean lower crust: Implications for zircon
864 geochronology, elemental and Sr-Nd-Hf isotopic geochemistry of late
865 Mesozoic granitoids from northwestern Jiaodong terrane, the North China
866 craton. *Lithos*, 146, 112-127.
- 867 Yang, L., Zhao, R., Wang, Q., Liu, X., Carranza, E.J.M. (2018) Fault geometry
868 and fluid-rock reaction: Combined controls on mineralization in the Xinli
869 gold deposit, Jiaodong Peninsula, China. *Journal of Structural Geology*,
870 111, 14-26.
- 871 Yang, L.Q., Deng, J., Wang, Z.L., Guo, L.N., Li, R.H., Groves, D.I.,
872 Danyushevskiy, L., Zhang, C., Zheng, X.L., Zhao, H. (2016) Relationships
873 between gold and pyrite at the Xincheng gold deposit, Jiaodong Peninsula,
874 China: implications for gold source and deposition in a brittle epizonal
875 environment. *Economic Geology*, 111, 105-126.
- 876 Zhang, C.Y. (2014) Pyrite genetic mineralogy and vertical contrast of the ultra-
877 deep drill of Sanshandao gold deposit in Jiaodong: Unpublished M.Sc.
878 thesis, Beijing, China, The University of Geosciences, 68p (in Chinese
879 with English abstract).
- 880 Zhu, R.X., Fan, H.R., Li, J.W., Meng, Q.R., Li, S.R., Zeng, Q.D. (2015)
881 Decratonic gold deposits. *Science China Earth Sciences*, 58, 1523-1537.

-
- 882 Zhu, Z.Y., Cook, N.J., Yang, T., Ciobanu, C., Zhao, K.D., Jiang, S.Y. (2016)
883 Mapping of sulfur isotopes and trace elements in sulfides by LA-(MC)-
884 ICP-MS: potential analytical problems, improvements and implications.
885 Minerals, 6, 110.
- 886 Zhu, Z.Y., Jiang, S.Y., Mathur, R., Cook, N.J., Yang, T., Wang, M., Ma, L.,
887 Ciobanu, C.L. (2018) Iron isotope behavior during fluid/rock interaction
888 in K-feldspar alteration zone—A model for pyrite in gold deposits from the
889 Jiaodong Peninsula, East China. *Geochimica et Cosmochimica Acta*, 222,
890 94-116.
- 891 Zoheir, B.A., El-Shazly, A.K., Helba, H., Khalil, K.I., Bodnar, R.J. (2008)
892 Origin and evolution of the Um Egat and Dungash orogenic gold deposits,
893 Egyptian Eastern Desert: evidence from fluid inclusions in quartz.
894 *Economic Geology*, 103, 405-424.
- 895

896 **Figure captions**

897 Figure 1. (a) Geologic map of Jiaodong Peninsula (after Fan et al., 2003). (b)
898 Geologic map of the Sanshandao Au deposit (after Wen et al., 2016). (c) Cross
899 section of the ZK96 prospecting line. (d) Three segments of drill holes of ZK96-
900 3, ZK96-6 and ZK96-5 showing the details of hydrothermal alterations, veins
901 and sampling information.

902

903 Figure 2. Photos of different types of mineralization and ore samples. (a)
904 Beresitization and quartz-pyrite (Py2) vein. (b) Quartz-pyrite vein in
905 beresitization zone. (c) Quartz-polysulfide vein and quartz-pyrite vein. (d) Hand
906 specimen of beresitization containing cataclastic quartz and fine-grained
907 sericite and Py1. (e) Curved quartz-pyrite vein in sericitization zone. (f) Quartz-
908 pyrite vein and quartz-polysulfide vein in sericitization zone.

909

910 Figure 3. Representative photomicrographs of visible gold grains and related
911 pyrite and other sulfide minerals. Numbers refer to fineness of individual spots
912 on Au grains. (a) Reflected light image of visible Au grains distributed on
913 boundaries of euhedral Py1. (b) Euhedral Py1 showing no zonation in BSE. (c)
914 Reflected light image of visible Au grains in fractures of anhedral Py2. (d) Py2
915 showing no BSE zonation. (e) Galena (reflected light) co-precipitated with
916 visible Au between pre-existing Py2. (f) Chalcopyrite (reflected light) co-
917 precipitated with visible Au between pre-existing Py2. (g) Visible Au (reflected

918 light) co-precipitated with Py₃, arsenopyrite and sphalerite. Inset shows BSE
919 zonation that distinguishes Py₃ and Py₃cr. (h) Reflected light image of large,
920 irregular-shaped Au grain, co-precipitated with arsenopyrite and galena. (i)
921 EDS elemental map of grains in panel (h), showing heterogeneity in distribution
922 of Au and Ag. (j) EDS elemental map of visible Au grain associated with Py₃
923 and sphalerite (one area in Fig. 7a) showing heterogeneous texture in
924 distribution of Au and Ag. (k) BSE image of Py₃cr co-precipitated with
925 polysulfides. Py₃ appears as BSE-bright rim around inclusion-rich Py₃cr core.
926 (l) Argentite co-precipitated with chalcopyrite and galena in a sample of the
927 deepest observed late generation Au mineralization.

928

929 Figure 4. Fineness of Au grains from early and late mineralization, relative to
930 depth in the deposit. Grey arrow highlights trend of decreasing fineness of Au
931 grains with decreasing depth.

932

933 Figure 5. LA-ICP-MS trace element results of pyrite. (a) Range and medians of
934 trace element contents of different pyrite, with calculated mean content added
935 for reference; the black horizontal bar is the mean detection limit. (b-c) Content
936 variations of different pyrite with depths for the elements of Co (b), Ni (c) and
937 As (d). Trace element concentrations below detection limit are plotted at half
938 the detection limit values.

939

940 Figure 6. Scatter diagrams of trace element for different pyrites. (a) Au vs. As;
941 (b) Au vs. Ag; (c) Au vs. Cu; (d) Au vs. Pb; (e) Bi vs. Pb; (f) Co vs. Ni. Trace
942 element concentrations below detection limit are plotted at half the detection
943 limit values.

944

945 Figure 7. LA-ICP-MS elemental maps of pyrite with core (Py3cr) and rim (Py3).
946 (a) BSE image of the pyrite. (b-f) Concentration scales are in ppm (logarithmic
947 10^n , where n is given on scale).

948

949 Figure 8. The range of sulfur isotope values of different generations of pyrite
950 and polysulfide minerals relative to depth in the deposit. Significance of grey
951 arrows is explained in text.

952

953 Figure 9. Schematic model for the temporal and spatial evolution of the
954 hydrothermal system at Sanshandao Au deposit, showing the depositional
955 mechanisms, controlling factors, variation of fineness, migrations of metals,
956 pyrite formations and hydrothermal alteration zones.

957

958 **Table captions**

959 Table 1. LA-ICP-MS trace elements results of MASS-1.

960

961 Table 2. EPMA fineness results of visible Au grains from different stages and

962 depths at Sanshandao deposit.

963

964 Table 3. Summarized LA-ICP-MS analytical results of selective elements for
965 different pyrites from different depths at Sanshandao deposit.

966

967 Table 4. LA-MC-ICP-MS analytical results of sulfur isotopic composition of
968 different sulfide from different depths at Sanshandao deposit.

969

970 **Electronic Supplemental materials**

971 Supplemental Table S1. EPMA results of visible Au grains from different stages
972 and depths at Sanshandao deposit.

973

974 Supplemental Table S2. LA-ICP-MS analytical results different pyrites from
975 different depths at Sanshandao deposit.

976

Table1. LA-ICP-MS trace element results of MASS-1.

	Co	Ni	Cu	Zn	As	Ag	Sb	Te	Au	Pb	Bi
Mean (ppm)	59.5	94.9	131000	188000	58.1	58.6	73.8	17.1	52.1	78.4	71.4
S.D. (n=22)	3.8	5.5	6300	12000	2.6	2.8	6.6	1.1	4.2	8.5	3.0
Preferred Values ¹	60	97	134000	210000	65	50	60	15	47	68	60
Preferred Values ²	67		134000	210000	65	67	55		47		7

S.D.= standard deviation

Preferred values1 is from the GeoRem database (<http://georem.mpch-mainz.gwdg.de>).

Preferred values2 is from Wilson et al. 2002.

Table 2. EPMA fineness results of visible gold grains from different stages and depths at Sanshandao deposit.

Sample No.	Associated sulfide	Depth (m)	Fineness	Sample No.	Associated sulfide	Depth (m)	Fineness	Sample No.	Associated sulfide	Depth (m)	Fineness
Early stage				ZK96-3-81		-1897	828	09S114-1	Py3-Sp	-800	608
10S22	Py1	-420	773	ZK96-3-81		-1897	828	09S114-1	Py3cr-Gn	-800	638
10S22		-420	746	ZK96-3-81		-1897	822	09S114-1	Py3cr	-800	638
10S22		-420	754				mean=855	09S114-1	Py3-Asp	-800	635
10S16	Py2	-420	757	ZK96-6-82	Py1	-2627	828	09S114-1	Py2-Asp	-800	660
10S16		-420	807	ZK96-6-82		-2627	828	09S114-2	Py2-Asp	-800	652
10S16		-420	742	ZK96-6-82		-2627	850	09S114-2	Py2-Asp	-800	626
10S16		-420	729	ZK96-6-82		-2627	855	09S114-2	Py2-Sp	-800	623
10S16		-420	743	ZK96-6-82		-2627	851	09S114-2	Py2-Gn	-800	588
10S16		-420	731	ZK96-6-82		-2627	839	09S114-2	Py2-Sp-Asp	-800	645
10S16		-420	743	ZK96-6-82		-2627	919	09S114-2	Py2-Sp-Gn	-800	630
10S16		-420	749	ZK96-6-82		-2627	923	09S114-2	Py2-Sp-Gn	-800	640
mean=752				ZK96-6-82		-2627	869	09S92	Py2-Gn	-800	624
09S74	Py1	-800	772	ZK96-6-82		-2627	854	09S92	Py2-Gn	-800	686
09S74		-800	763	ZK96-6-82		-2627	826	09S92	Py2-Gn	-800	686
09S74		-800	779	ZK96-6-82		-2627	850	09S92	Py2-Gn	-800	683
09S74		-800	763	ZK96-6-82		-2627	857	09S92	Py2-Gn	-800	549
09S94		-800	776	ZK96-6-79	Py2	-2613	859	09S92	Py2-Gn	-800	654
09S94		-800	780	ZK96-6-79		-2613	869	09S92	Py2-Gn	-800	684
09S94		-800	751	ZK96-6-79		-2613	849	09S92	Py2-Sp	-800	719
09S37	Py2	-800	809	ZK96-6-79		-2613	846	09S92	Py2-Sp	-800	719
09S37		-800	802	ZK96-6-79		-2613	961	09S93	Py2-Ccp	-800	666
09S37		-800	859	ZK96-6-84		-2636	917	09S93	Py2-Ccp	-800	643
mean=785				ZK96-6-84		-2636	919	09S93	Py2-Ccp	-800	698
ZK96-3-70	Py1	-1855	860	ZK96-6-84		-2636	895	09S119	Py2-Gn-Asp	-800	696
ZK96-3-70		-1855	852	ZK96-6-84		-2636	912	09S119	Py2-Gn-Asp	-800	689
ZK96-3-70		-1855	835	ZK96-6-84		-2636	868	09S119	Py2-Gn-Asp	-800	673
ZK96-3-70		-1855	925	ZK96-6-84		-2636	906	mean=654			
ZK96-3-70		-1855	795	ZK96-6-84		-2636	878	ZK96-3-53	Ccp	-1448	672
ZK96-3-72		-1866	817	ZK96-6-84		-2636	870	ZK96-3-53	Py2-Ccp	-1448	667
ZK96-3-72		-1866	919	ZK96-6-85		-2650	850	ZK96-3-53	Py2-Ccp	-1448	623
ZK96-3-72		-1866	921	ZK96-6-85		-2650	865	ZK96-3-53	Py2-Ccp	-1448	687
ZK96-3-72		-1866	806	ZK96-6-85		-2650	831	ZK96-3-53	Py2-Ccp	-1448	680
ZK96-3-72		-1866	858	ZK96-6-85		-2650	841	ZK96-3-54	Py2-Ccp	-1448	665
ZK96-3-72		-1866	939				mean=870	ZK96-3-54	Py2-Ccp	-1448	693
ZK96-3-75	Py2	-1880	853	Late stage				mean=670			
ZK96-3-75		-1880	844	10S23	Asp	-420	658	10S21	Py3-Sp	-420	421
ZK96-3-75		-1880	941	10S23	Asp	-420	644	09S114-1	Py2-Gn-Asp	-800	263
ZK96-3-75		-1880	869	10S23	Asp	-420	618	09S119	Py2-Gn-Asp	-800	348
ZK96-3-75		-1880	826	10S23	Asp-Sp	-420	709	09S119	Py2-Gn-Asp	-800	218
ZK96-3-81		-1897	841	10S23	Asp	-420	635	09S119	Py2-Gn-Asp	-800	233
ZK96-3-81		-1897	824	10S16	Py2-Gn	-420	638	09S119	Py2-Gn-Asp	-800	417
ZK96-3-81		-1897	872	10S16	Py2-Gn	-420	659	mean=317			
ZK96-3-81		-1897	821	10S21	Py3-Sp	-420	634				
ZK96-3-81		-1897	830				mean=649				

Table 3. Summarized LA-ICP-MS analytical results of selective elements for different pyrites from different depths at Sanshandao deposit.

	Co	Ni	Cu	Zn	As	Ag	Sb	Te	Au	Pb	Bi
Py1 (-3537 ~ -3739m; n=5)											
Median	247	617	34.1	bdl	7.2	6.8	0.7	bdl	bdl	76.9	0.5
MAD	154	523	33.6	1.2	4.5	2.1	0.7	0.7	0.1	37.9	0.5
Min	92.5	93.9	bdl	bdl	2.7	bdl	bdl	bdl	bdl	bdl	bdl
Max	2770	3900	294	11.6	671	11.6	3.6	20.0	0.3	122	61.4
Py1 (-2516 ~ -2627m; n=8)											
Median	94.0	507	17.5	bdl	253	4.8	0.2	4.7	0.1	116	44.4
MAD	74.7	87.4	7.2	0.2	176	4.6	0.1	4.0	0.1	56.3	37.3
Min	19.3	18.6	bdl	bdl	4.9	bdl	bdl	bdl	bdl	1.0	2.7
Max	420	594	39.8	3.0	506	18.8	1.6	24.1	1.6	172	99.2
Py1 (-1855 ~ -1875m; n=8)											
Median	29.0	3.1	bdl	bdl	894	bdl	bdl	bdl	bdl	1.0	0.9
MAD	22.2	1.7	0.1	0.2	827	0.1	0.0	0.3	0.0	1.0	0.8
Min	0.6	0.8	bdl	bdl	11.4	bdl	bdl	bdl	bdl	bdl	0.1
Max	92.0	83.5	3.8	bdl	2610	2.1	0.2	4.7	0.5	9.0	23.5
Py1 (-420 ~ -800m; n=13)											
Median	2.6	2.5	3.2	bdl	864	2.2	0.2	4.4	0.1	8.7	10.6
MAD	2.5	2.3	1.3	0.2	357	1.9	0.2	3.6	0.1	7.4	6.2
Min	0.1	bdl	bdl	bdl	1.7	bdl	bdl	bdl	bdl	0.5	0.1
Max	171	222	26.1	7.0	2500	9.0	3.3	16.7	0.6	65.7	32.7
Py1 (all: -420 ~ -3739m; n=33)											
Median	46.0	19.6	3.2	bdl	512	2.1	0.2	2.5	0.1	8.7	10.2
MAD	45.2	19.4	2.8	0.3	460	2.0	0.1	2.0	0.1	8.2	9.6
Min	0.1	bdl	bdl	bdl	1.7	bdl	bdl	bdl	bdl	bdl	bdl
Max	2770	3900	294	11.6	2610	18.8	3.6	24.1	1.6	172	99.2
Py2 (-3633 ~ -3798m; n=8)											
Median	1330	158	0.8	bdl	3.5	bdl	bdl	bdl	bdl	0.6	1.0
MAD	1100	25.2	0.5	0.2	3.0	0.0	0.0	0.2	0.0	0.5	0.9
Min	83.5	64.8	bdl	bdl	bdl	bdl	bdl	bdl	bdl	bdl	bdl
Max	2900	257	24.9	1.8	28.4	8.5	1.4	21.5	0.3	254	55.0
Py2 (-2613 ~ -2680m; n=8)											
Median	14.8	28.9	6.6	bdl	90.4	3.7	0.1	7.4	0.6	29.2	17.6
MAD	6.2	10.1	6.0	0.3	28.6	3.5	0.1	5.1	0.5	27.9	16.1
Min	5.9	2.1	0.7	bdl	14.3	0.1	bdl	bdl	bdl	0.8	0.4
Max	103	92.9	36.2	1.8	252	16.3	0.8	37.7	1.2	307	91.5
Py2 (-1448 ~ -1909m; n=9)											
Median	5.5	1.7	bdl	bdl	64.3	0.3	bdl	bdl	bdl	0.7	8.7
MAD	2.5	1.5	0.1	0.2	62.2	0.3	0.0	0.5	0.0	0.6	8.6
Min	0.3	bdl	bdl	bdl	1.1	bdl	bdl	bdl	bdl	bdl	0.0
Max	12.2	46.7	8.4	3.8	1220	19.8	1.8	2.0	0.8	35.6	28.8
Py2 (-420 ~ -800m; n=20)											
Median	1.8	0.4	8.8	1.4	40.9	5.7	0.7	bdl	bdl	14.3	1.1
MAD	1.8	0.2	8.2	0.8	31.7	5.6	0.6	0.4	0.0	11.9	1.1
Min	bdl	bdl	bdl	bdl	4.9	bdl	bdl	bdl	bdl	0.1	bdl
Max	21.0	34.5	83.0	63.7	706	76.9	4.4	6.1	0.2	98.4	16.6
Py2 (all: -420 ~ -3798m; n=45)											

Median	8.0	10.3	1.7	bdl	41.7	2.6	0.2	bdl	bdl	5.4	2.4
MAD	7.7	10.1	1.5	0.4	38.1	2.5	0.1	0.4	0.0	5.3	2.3
Min	bdl	bdl	bdl	bdl	bdl	bdl	bdl	bdl	bdl	bdl	bdl
Max	2900	257	83.0	63.7	1220	76.9	4.4	37.7	1.2	307	91.5
Py3cr (-420 ~ -800m; n=24)											
Median	bdl	bdl	4.6	1.6	8.6	0.9	0.8	bdl	bdl	14.1	bdl
MAD	0.0	0.0	4.3	0.9	8.1	0.8	0.7	0.2	0.0	13.5	0.0
Min	bdl	bdl	bdl	bdl	bdl	bdl	bdl	bdl	bdl	bdl	bdl
Max	0.3	bdl	169	75.9	446	41.7	28.6	bdl	0.6	189	0.2
Py3 (-420 ~ -800m; n=29)											
Median	bdl	bdl	2.0	1.1	10000	0.8	1.2	bdl	2.2	7.6	bdl
MAD	0.0	0.0	1.2	0.5	2230	0.6	0.9	0.2	1.3	6.0	0.0
Min	bdl	bdl	bdl	bdl	1700	bdl	bdl	bdl	0.2	bdl	bdl
Max	1.5	1.1	25.6	9.5	16300	15.2	8.5	bdl	19.6	60.4	0.1

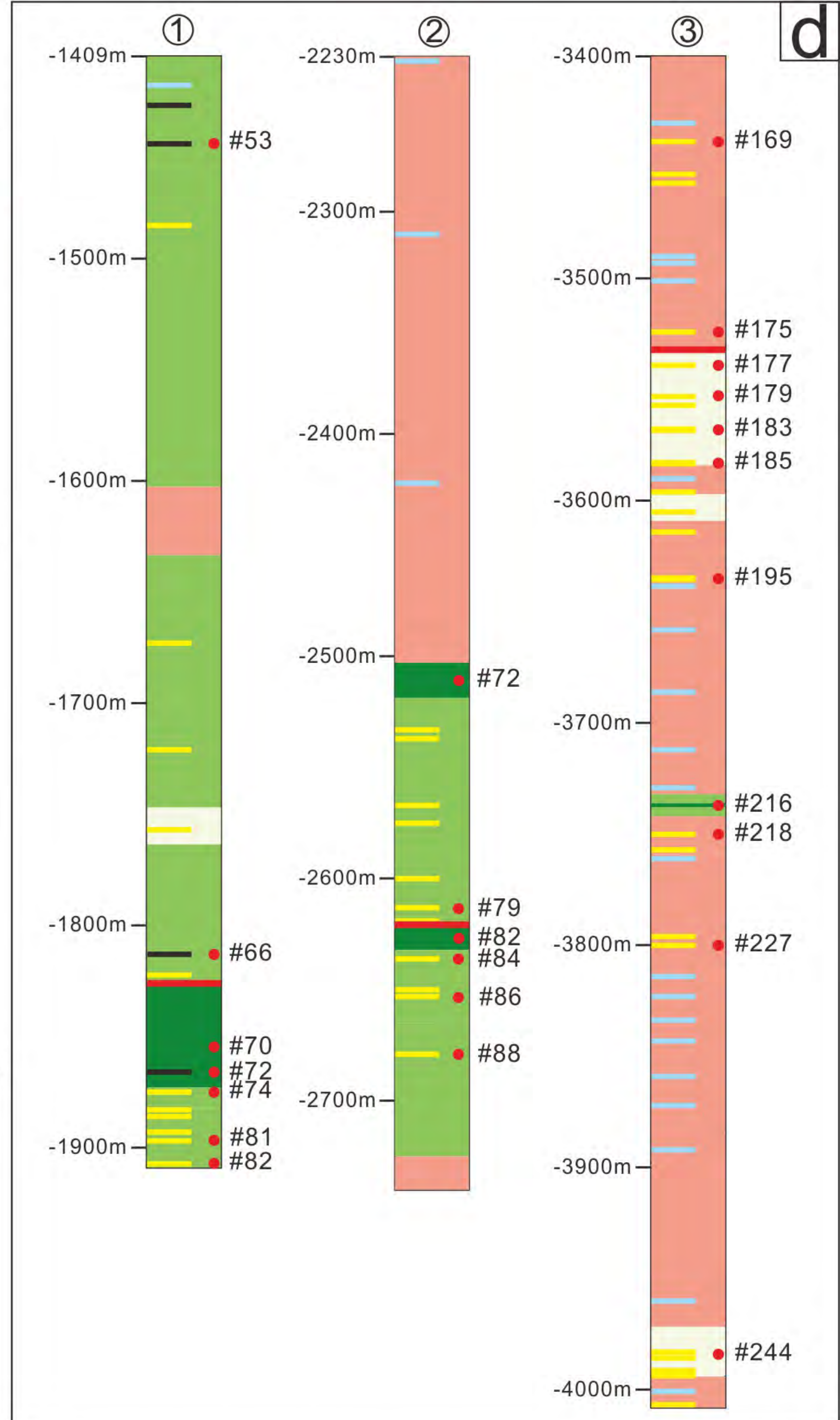
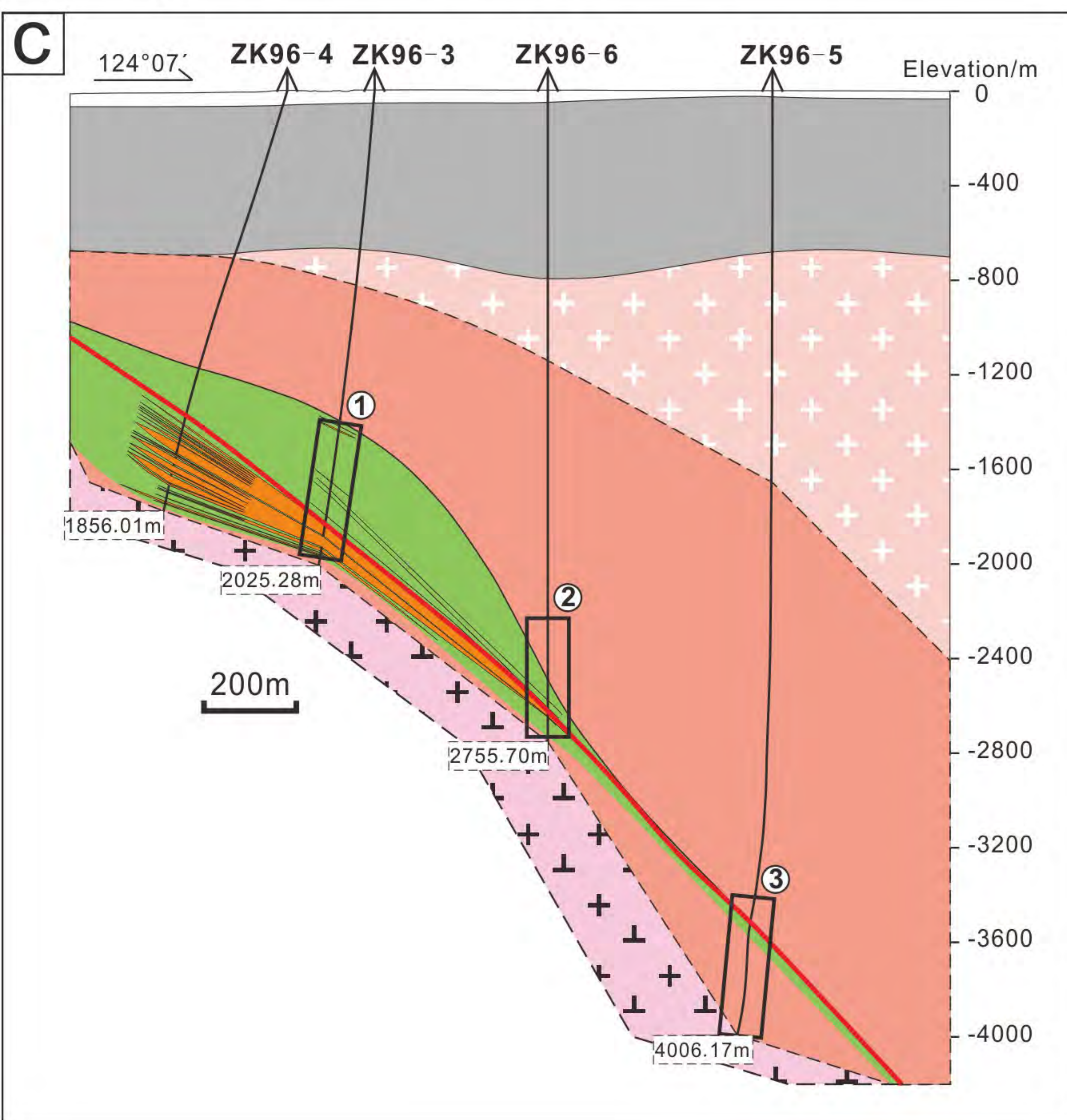
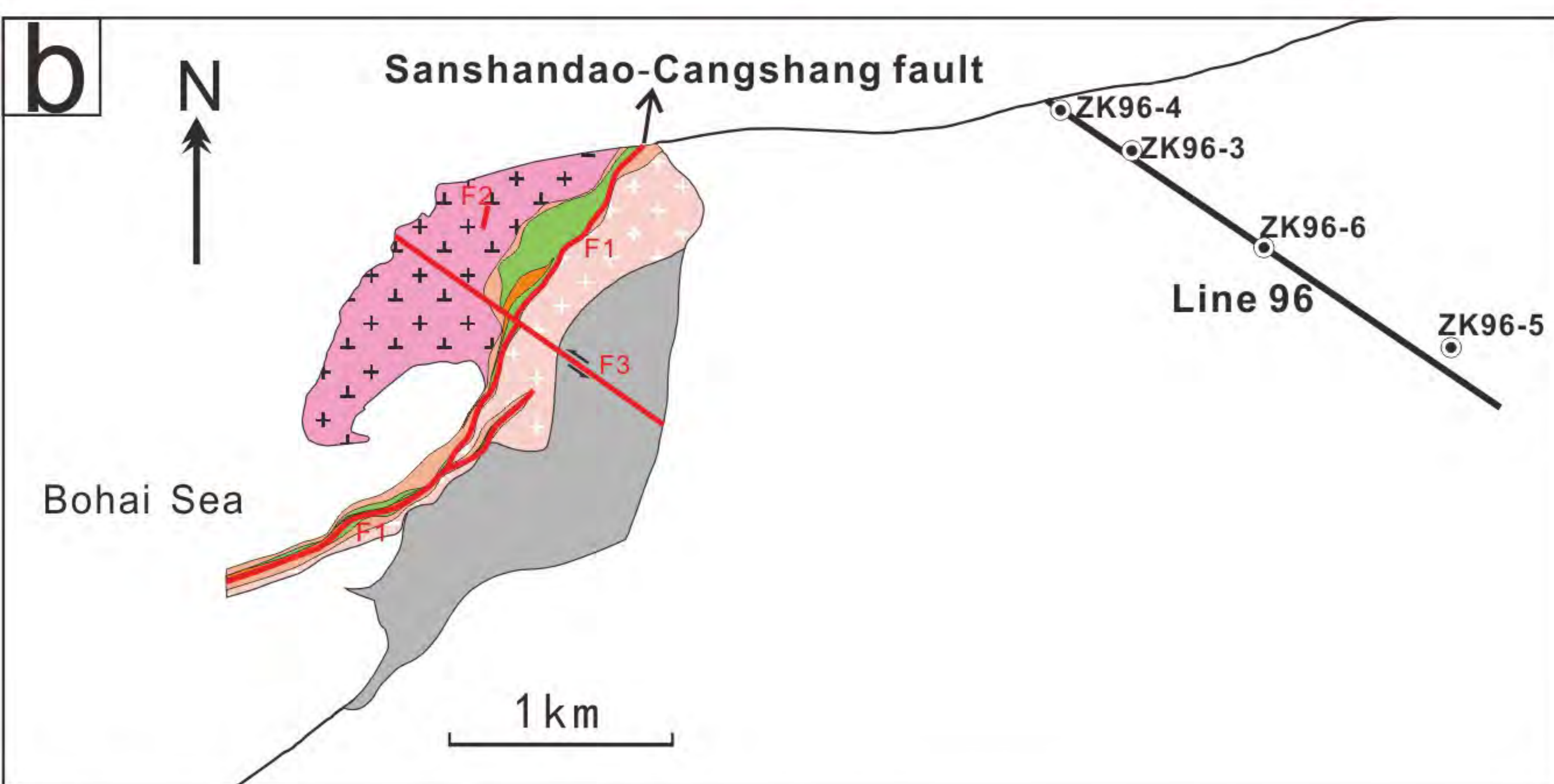
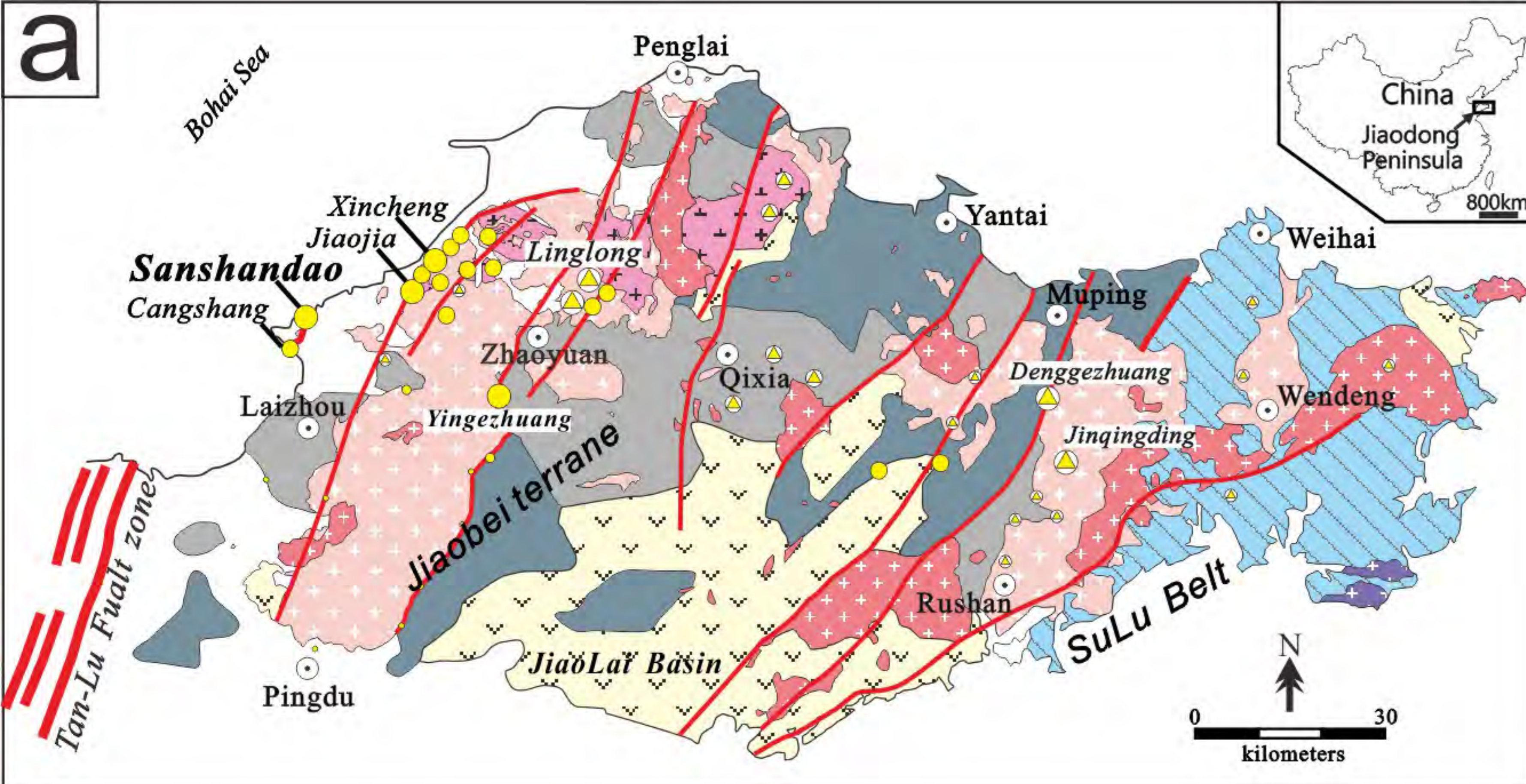
MAD = median absolute deviation

bdl = below detection limit

Table 4. LA-MC-ICP-MS analytical results of sulfur isotopic composition of different sulfide from different depths at Sanshandao deposit.

Sample No.	Depth (m)	$^{34}\text{S}/^{32}\text{S}$	$\delta^{34}\text{S}\text{‰}$	Sample No.	Depth (m)	$^{34}\text{S}/^{32}\text{S}$	$\delta^{34}\text{S}\text{‰}$	Sample No.	Depth (m)	$^{34}\text{S}/^{32}\text{S}$	$\delta^{34}\text{S}\text{‰}$
Py1				ZK96-5-185	-3581	0.049343	4.9	Py3			
ZK96-5-177	-3537	0.049571	9.9	ZK96-5-185	-3581	0.049358	5.2	09S114-1	-800	0.049628	10.4
ZK96-5-177	-3537	0.049592	10.5	ZK96-5-185	-3581	0.049350	5.1	09S114-1	-800	0.049621	10.3
ZK96-5-177	-3537	0.049590	10.4	ZK96-5-169	-3437	0.049221	2.5	09S114-1	-800	0.049626	10.5
ZK96-5-177	-3537	0.049570	10.1	ZK96-5-169	-3437	0.049220	2.4	09S114-1	-800	0.049641	10.8
ZK96-5-177	-3537	0.049574	10.0	ZK96-5-169	-3437	0.049291	3.9	09S114-1	-800	0.049611	10.2
ZK96-5-216	-3739	0.049579	10.1	ZK96-5-169	-3437	0.049236	2.7	09S114-1	-800	0.049633	10.6
ZK96-5-216	-3739	0.049633	11.2	ZK96-5-169	-3437	0.049256	3.2	09S114-1	-800	0.049626	10.3
ZK96-5-216	-3739	0.049631	11.2	ZK96-5-169	-3437	0.049230	1.7	09S114-1	-800	0.049635	10.4
ZK96-5-216	-3739	0.049587	10.3	ZK96-5-169	-3437	0.049223	1.6	09S114-1	-800	0.049629	10.8
ZK96-5-216	-3739	0.049571	10.0	ZK96-5-169	-3437	0.049222	1.5	09S114-1	-800	0.049634	10.9
ZK96-5-216	-3739	0.049653	11.2	mean = 3.1			09S25	-800	0.049585	9.6	
ZK96-5-218	-3748	0.049634	10.8	ZK96-6-79	-2613	0.049586	9.7	09S25	-800	0.049605	10.0
ZK96-5-218	-3748	0.049637	10.9	ZK96-6-79	-2613	0.049548	9.5	09S25	-800	0.049602	9.9
mean = 10.5				ZK96-6-79	-2613	0.049619	10.9	09S25	-800	0.049598	9.9
ZK96-6-72	-2516	0.049638	11.1	ZK96-6-84	-2636	0.049597	10.3	09S25	-800	0.049597	9.8
ZK96-6-72	-2516	0.049653	11.4	ZK96-6-84	-2636	0.049589	10.3	09S25	-800	0.049601	10.1
ZK96-6-72	-2516	0.049657	11.5	ZK96-6-86	-2652	0.049585	10.2	09S25	-800	0.049611	10.3
ZK96-6-72	-2516	0.049622	10.8	ZK96-6-86	-2652	0.049604	9.6	09S25	-800	0.049609	10.3
ZK96-6-82	-2627	0.049614	10.8	ZK96-6-88	-2680	0.049608	9.7	10S21	-420	0.049623	10.5
ZK96-6-82	-2627	0.049643	11.8	ZK96-6-88	-2680	0.049605	11.0	10S21	-420	0.049616	10.2
ZK96-6-82	-2627	0.049645	11.1	mean = 10.1			10S21	-420	0.049660	11.1	
ZK96-6-82	-2627	0.049601	10.4	ZK96-3-53	-1448	0.049610	10.0	mean = 10.3			
mean = 11.1				ZK96-3-53	-1448	0.049607	9.9	Gn			
ZK96-3-70	-1855	0.049618	10.5	ZK96-3-66	-1813	0.049600	9.7	ZK96-5-179	-3551	0.049471	6.7
ZK96-3-70	-1855	0.049633	10.9	ZK96-3-66	-1813	0.049553	9.7	ZK96-5-179	-3551	0.049461	6.5
ZK96-3-70	-1855	0.049659	12.1	ZK96-3-74	-1875	0.049558	9.9	ZK96-6-86	-2652	0.049476	7.2
ZK96-3-72	-1866	0.049628	10.6	ZK96-3-74	-1875	0.049554	9.8	ZK96-6-86	-2652	0.049487	7.6
ZK96-3-72	-1866	0.049668	11.4	ZK96-3-81	-1897	0.049509	9.1	ZK96-3-53	-1448	0.049238	3.5
ZK96-3-72	-1866	0.049708	12.2	ZK96-3-81	-1897	0.049510	9.1	ZK96-3-53	-1448	0.049338	4.4
ZK96-3-74	-1875	0.049657	11.9	ZK96-3-81	-1897	0.049577	10.5	ZK96-3-66	-1813	0.049362	4.9
ZK96-3-74	-1875	0.049645	11.5	ZK96-3-82	-1909	0.049591	10.7	09S92	-800	0.049421	6.7
mean = 11.4				ZK96-3-82	-1909	0.049535	9.6	09S92	-800	0.049434	7.0
09S74	-800	0.049662	11.8	ZK96-3-82	-1909	0.049641	10.2	10S16	-420	0.049465	7.3
09S74	-800	0.049673	12.0	mean = 9.8			10S16	-420	0.049459	7.3	
09S74	-800	0.049657	11.7	09S92	-800	0.049583	10.0	Ccp			
09S94	-800	0.049631	11.3	09S92	-800	0.049569	9.7	ZK96-6-86	-2652	0.049545	8.4
09S94	-800	0.049631	11.3	09S92	-800	0.049567	9.7	ZK96-6-86	-2652	0.049505	8.1
09S94	-800	0.049633	11.3	09S92	-800	0.049583	9.8	ZK96-3-53	-1448	0.049332	5.5
10S22	-420	0.049731	12.7	09S135	-800	0.049619	10.9	ZK96-3-53	-1448	0.049338	5.6
10S22	-420	0.049656	11.8	09S135	-800	0.049620	10.9	ZK96-3-53	-1448	0.049350	5.8
10S22	-420	0.049668	12.1	10S16	-420	0.049616	10.4	ZK96-3-66	-1813	0.049511	8.8
mean = 11.8				10S16	-420	0.049622	10.5				
				10S16	-420	0.049603	10.1				

Py2				Py3cr				Sp				Apy			
ZK96-5-175	-3522	0.049560	9.7	10S16	-420	0.049599	10.0	ZK96-3-66	-1813	0.049514	8.0				
ZK96-5-175	-3522	0.049541	9.3	10S23	-420	0.049572	9.5	ZK96-3-82	-1909	0.049546	9.5				
ZK96-5-175	-3522	0.049574	10.0	10S23	-420	0.049598	10.5	ZK96-3-82	-1909	0.049569	10.0				
ZK96-5-179	-3551	0.049518	9.0	mean = 10.2				09S92	-800	0.049613	10.8				
ZK96-5-179	-3551	0.049528	9.2	Py3cr				10S16	-420	0.049574	9.7				
ZK96-5-183	-3566	0.049638	10.1	09S114-1	-800	0.049561	9.0	Sp							
ZK96-5-183	-3566	0.049581	10.2	09S114-1	-800	0.049570	9.2	ZK96-3-53	-1448	0.049372	6.2				
ZK96-5-195	-3633	0.049563	9.8	09S114-1	-800	0.049584	9.5	ZK96-3-53	-1448	0.049358	6.0				
ZK96-5-195	-3633	0.049555	9.6	09S114-1	-800	0.049575	9.4	09S114-1	-800	0.049601	10.5				
ZK96-5-218	-3748	0.049511	8.6	09S114-1	-800	0.049560	9.1	09S114-1	-800	0.049572	9.9				
ZK96-5-218	-3748	0.049506	8.5	09S114-1	-800	0.049585	9.6	09S114-1	-800	0.049563	9.7				
ZK96-5-218	-3748	0.049498	8.2	09S114-1	-800	0.049561	8.9	10S23	-420	0.049584	10.2				
ZK96-5-227	-3798	0.049551	9.6	09S114-1	-800	0.049559	8.9	10S23	-420	0.049569	9.9				
ZK96-5-227	-3798	0.049578	10.1	09S114-1	-800	0.049591	10.0	Apy							
ZK96-5-227	-3798	0.049573	10.0	09S114-1	-800	0.049585	9.9	09S114-1	-800	0.049597	9.7				
ZK96-5-227	-3798	0.049575	10.0	09S25	-800	0.049541	8.7	09S114-1	-800	0.049592	10.0				
ZK96-5-244	-3982	0.049580	10.2	09S25	-800	0.049545	8.8	09S25	-800	0.049578	9.4				
ZK96-5-244	-3982	0.049556	9.7	09S25	-800	0.049538	8.6	09S25	-800	0.049566	9.2				
ZK96-5-244	-3982	0.049574	10.0	09S25	-800	0.049555	9.2	09S25	-800	0.049577	9.4				
ZK96-5-244	-3982	0.049516	8.8	10S21	-420	0.049586	9.7	09S25	-800	0.049577	9.4				
ZK96-5-244	-3982	0.049586	10.3	10S21	-420	0.049565	9.2	10S23	-420	0.049596	10.5				
mean = 9.6				10S21	-420	0.049589	9.6	10S21	-420	0.049595	9.9				
mean = 9.3															



Precambrian and Phanerozoic formations

- Quaternary sediments
- Early Cretaceous sedimentary and volcanic rocks
- UHP metamorphic rocks
- Proterozoic metamorphic rocks
- Archean metamorphic rocks

Mesozoic granitic rocks

- Early Cretaceous AiShan Cretaceous granites
- Early Cretaceous Guojialing granodiorite
- Late Jurassic Linglong granite
- Late Triassic granitoids

Deposit and fault

- Disseminated-type gold deposit
- Vein-type gold deposit
- Orebody
- Fault

Veins and sample locations

- Quartz-polysulfide vein
- Quartz-pyrite vein
- Quartz vein
- Sample

Alteration rocks

- Beresitization
- Silicification
- Sericitization
- K-feldspar alteration

Fig. 1

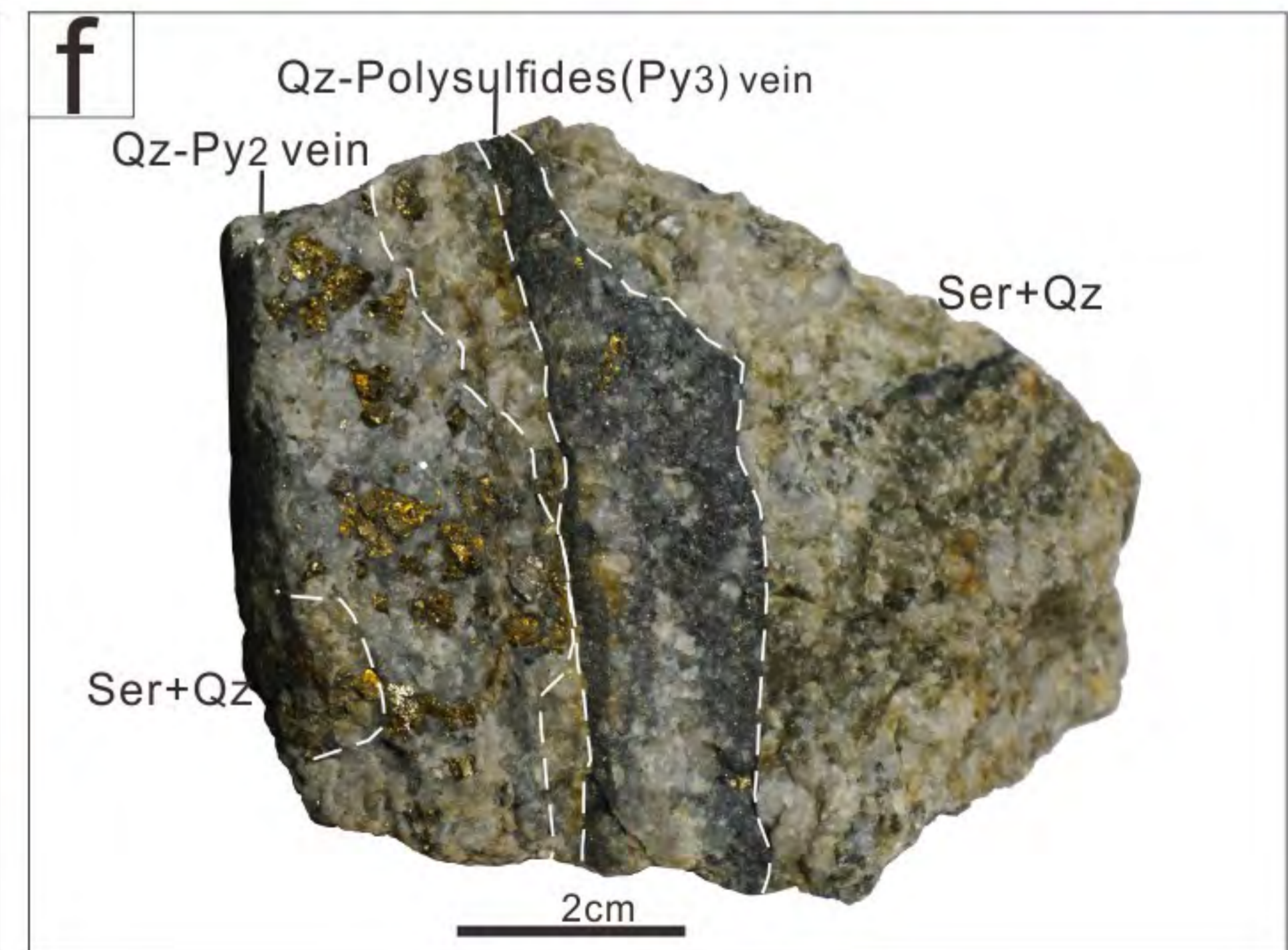
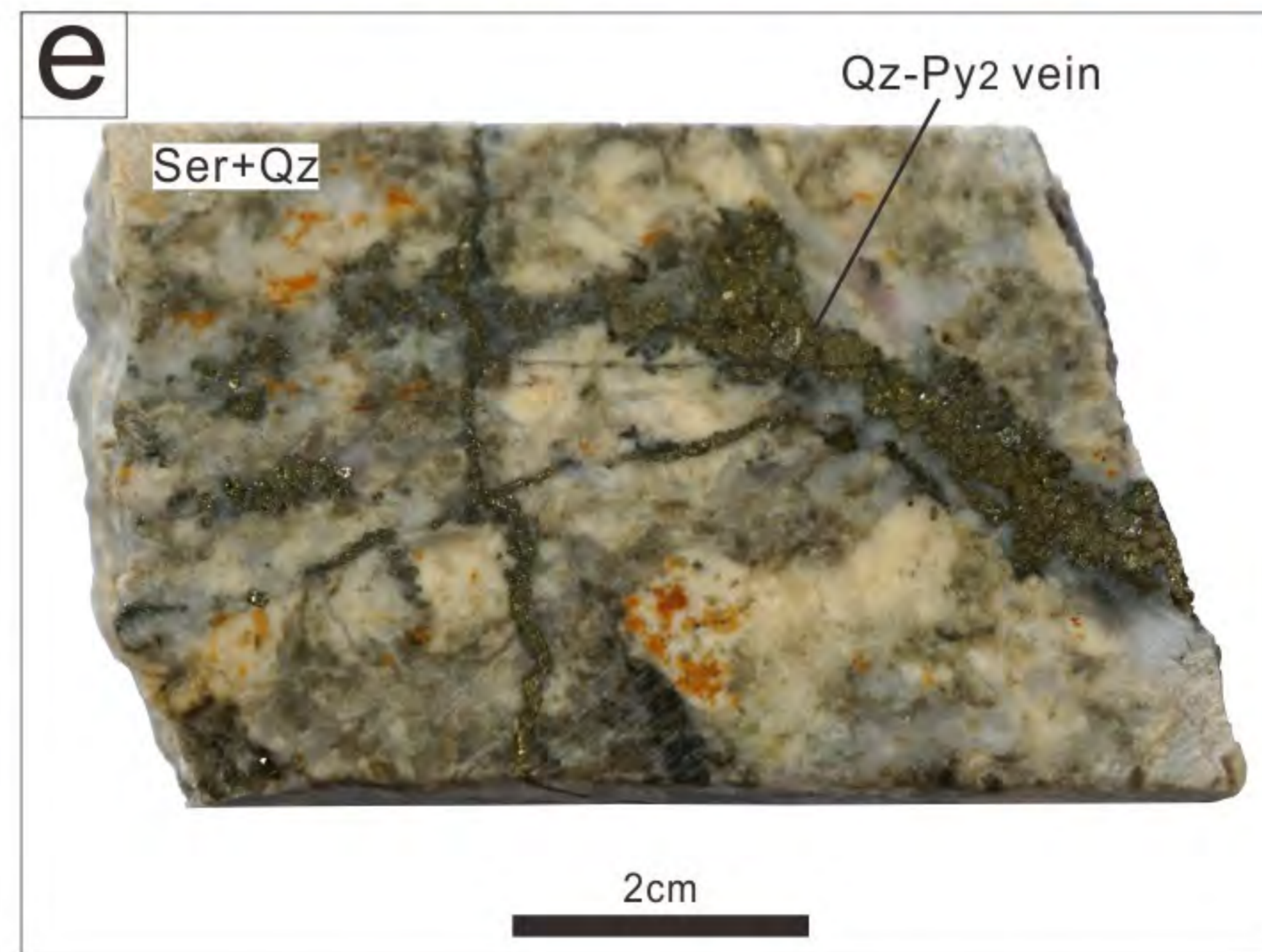
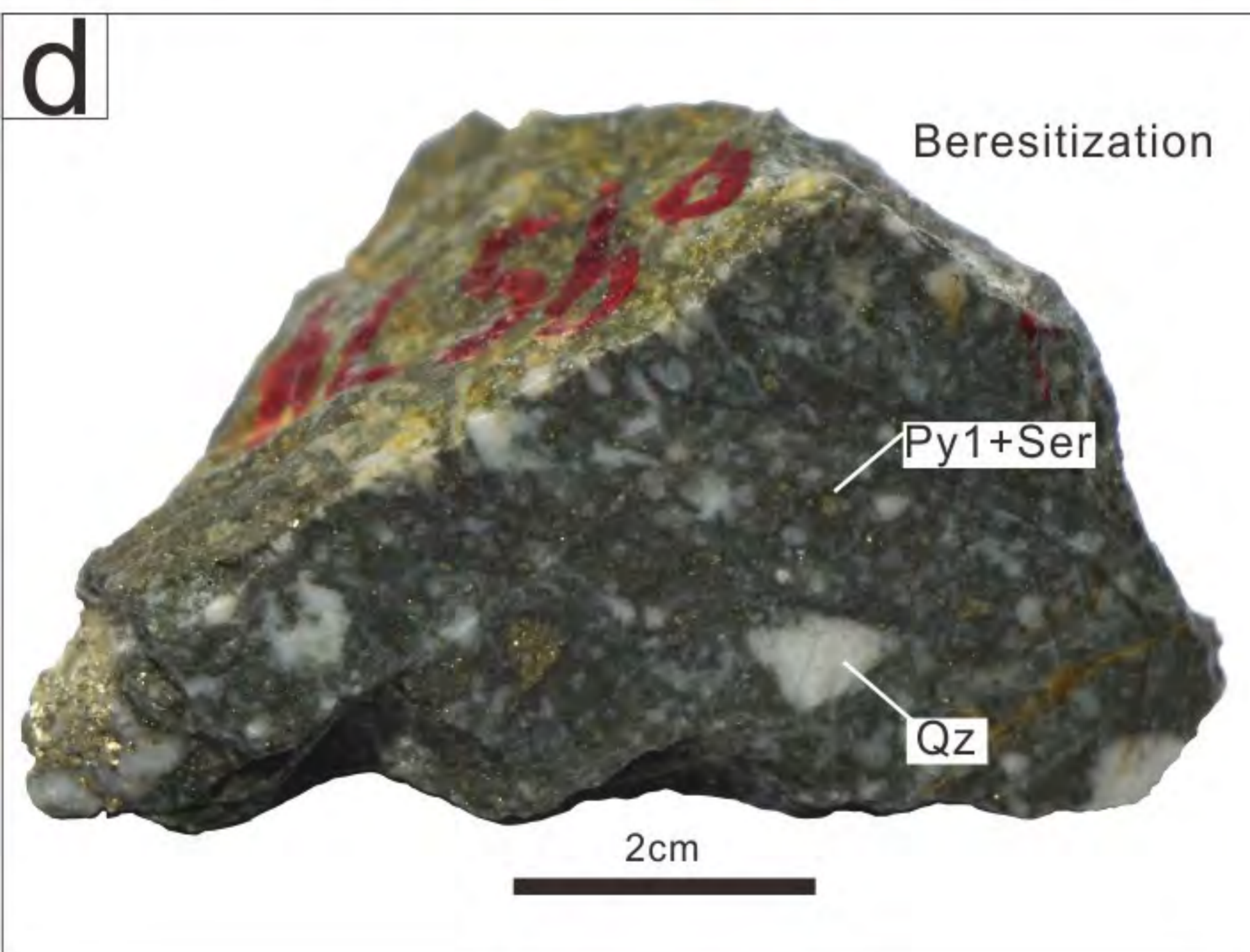
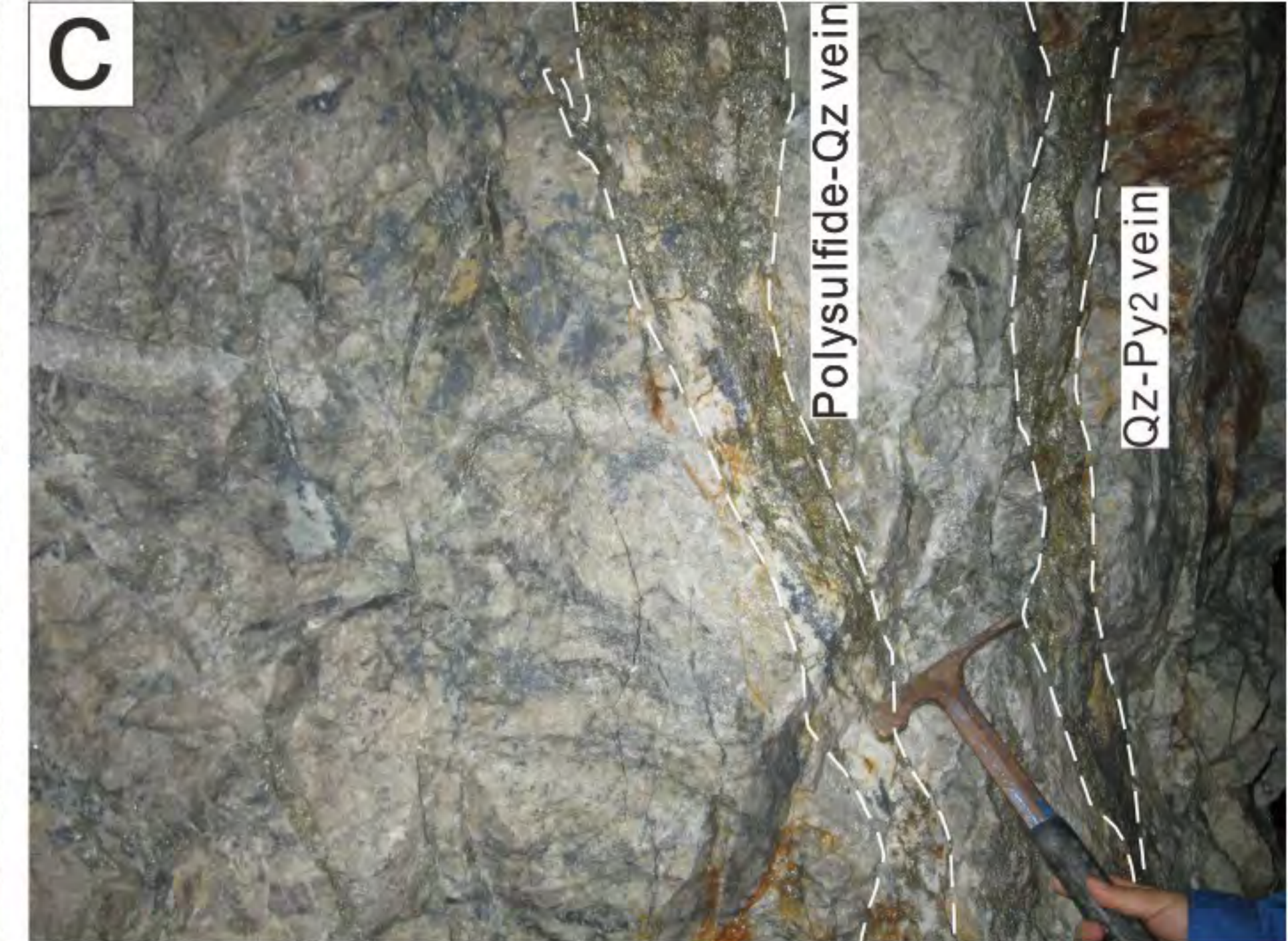
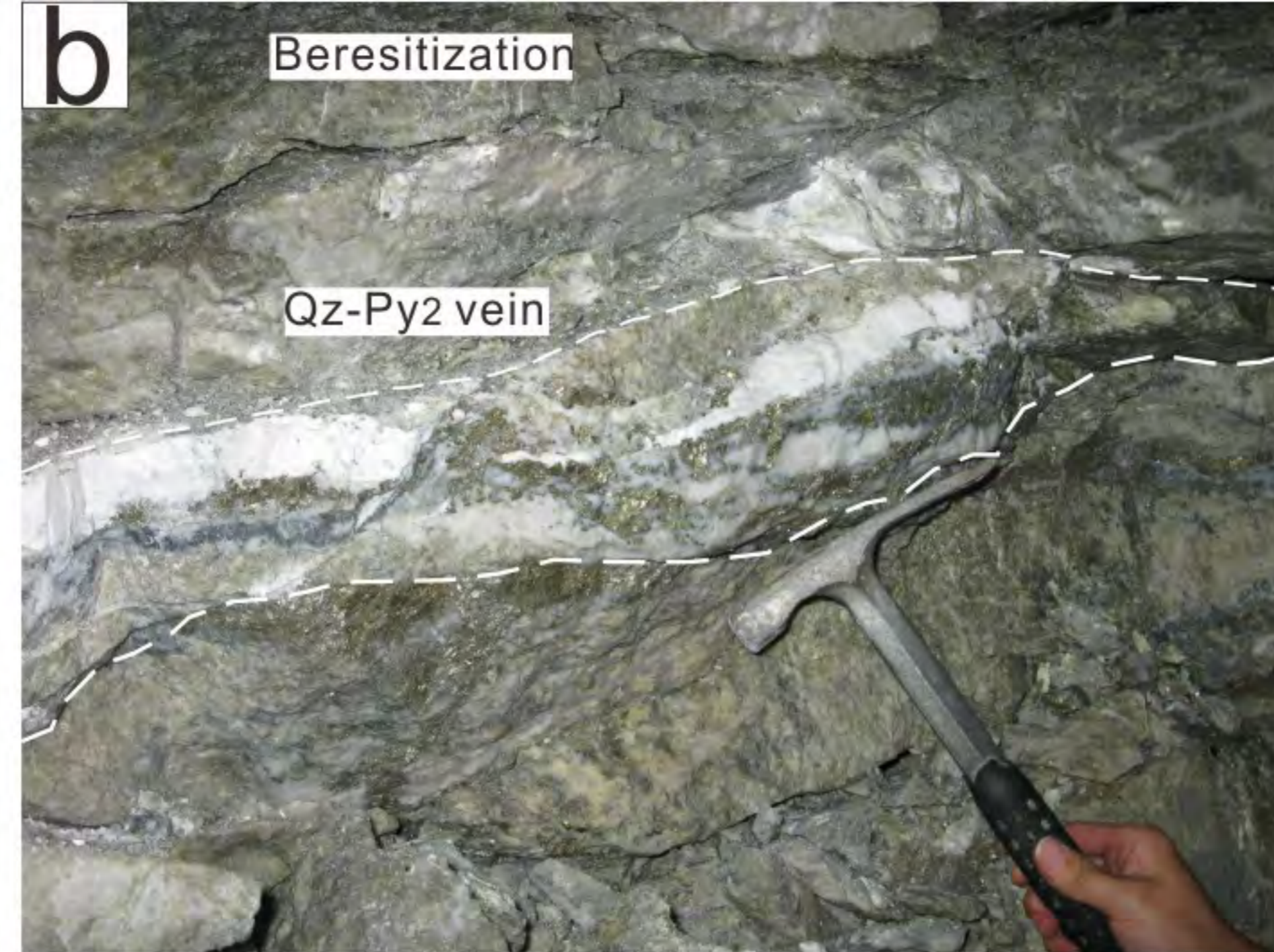
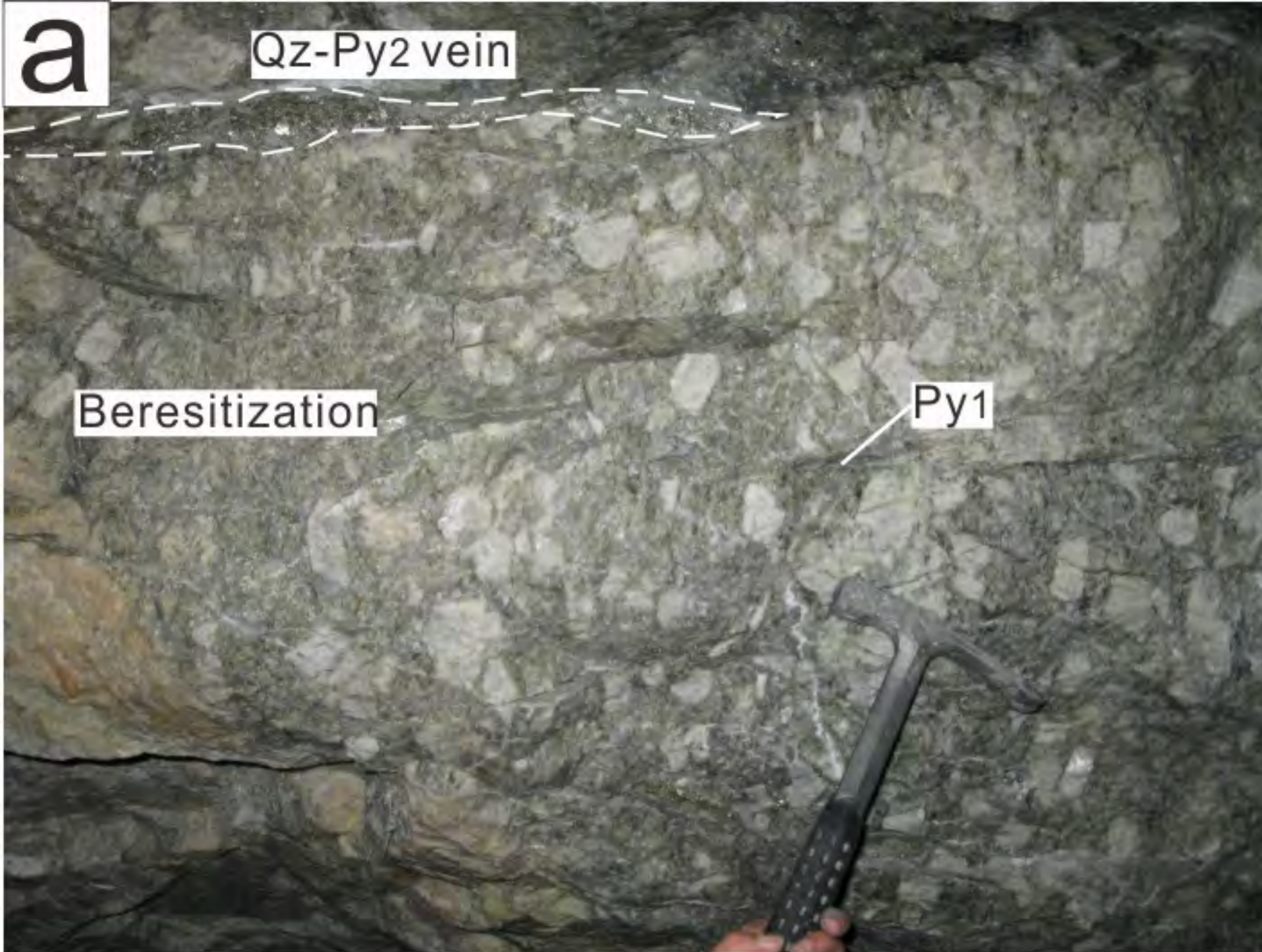


Fig. 2

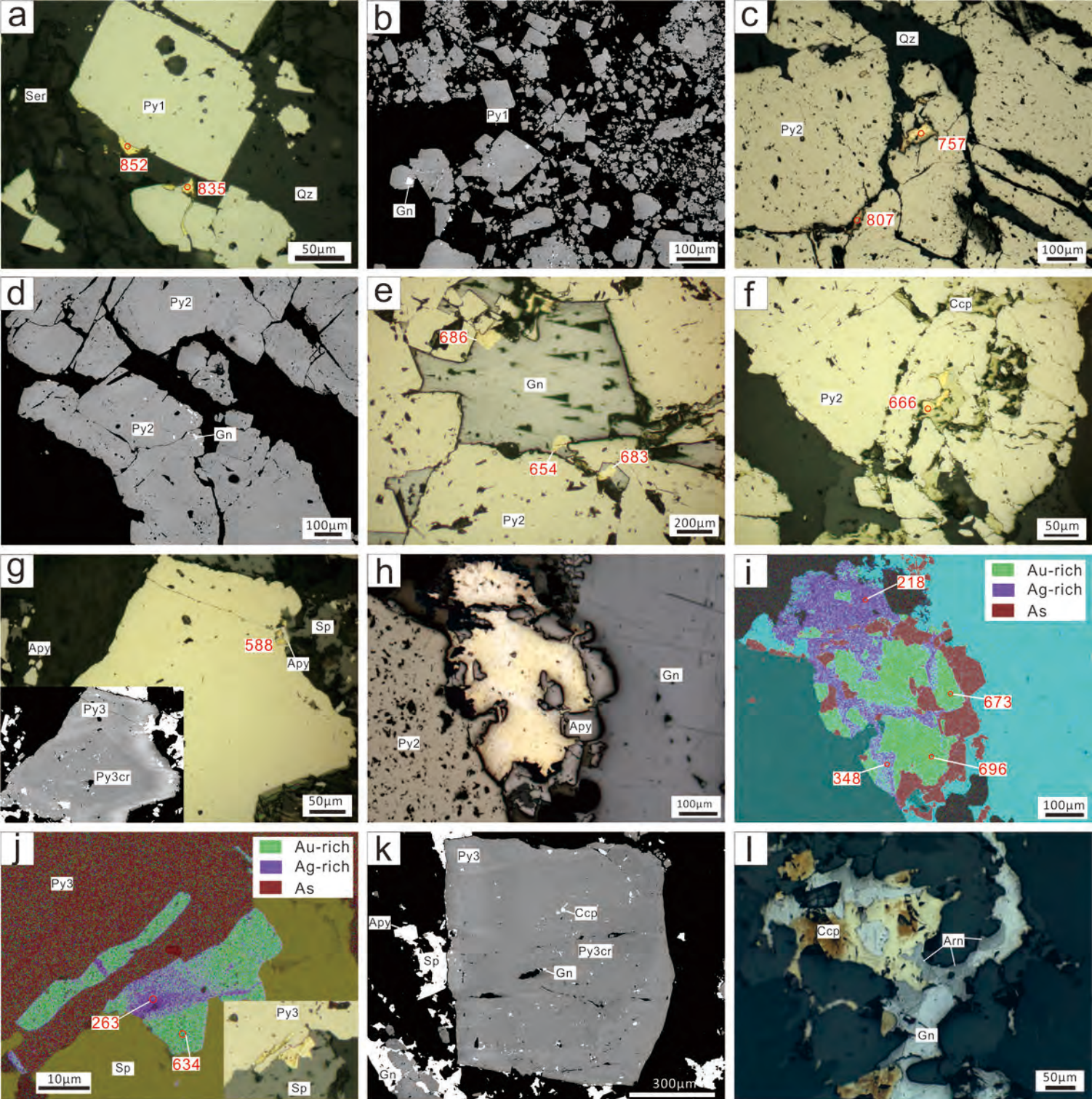


Fig. 3

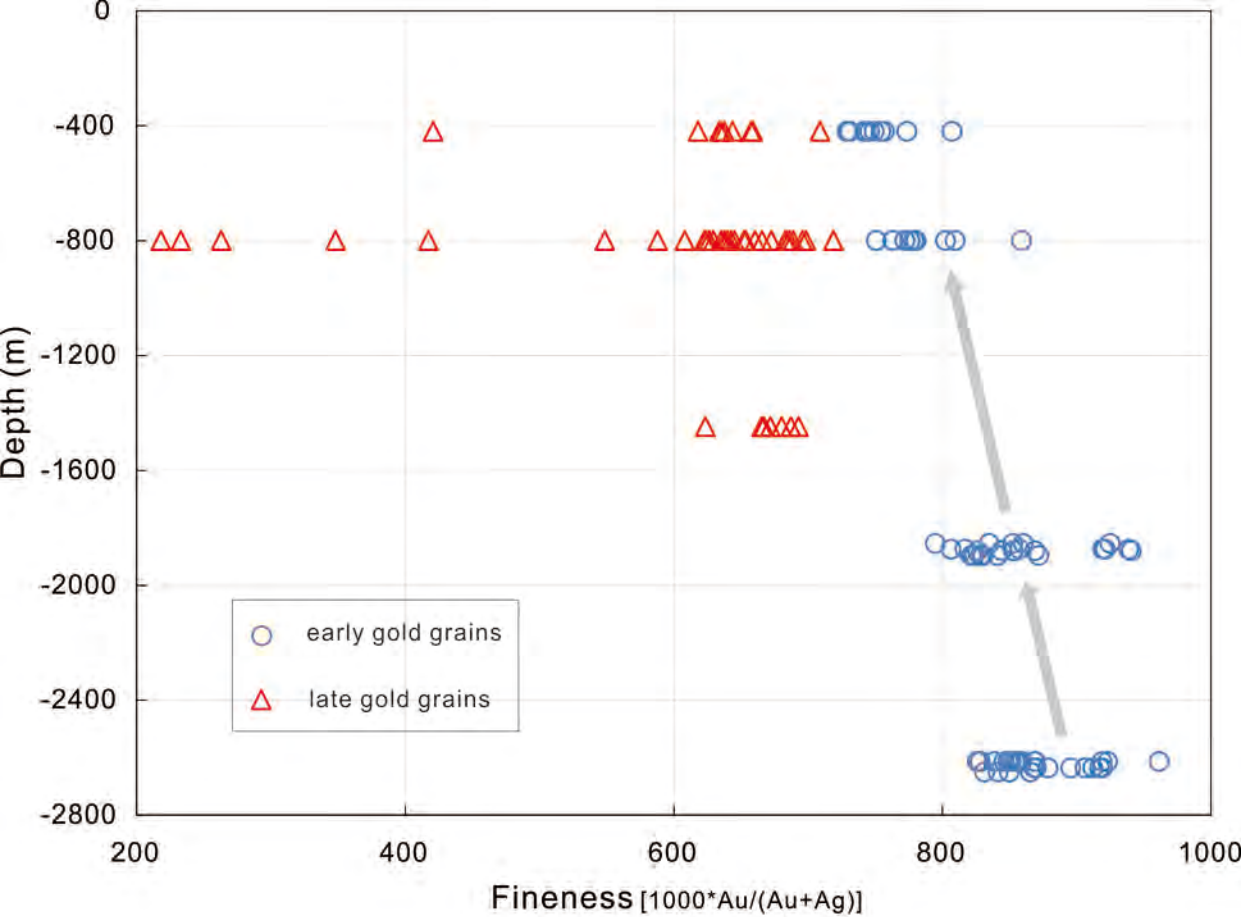


Fig. 4

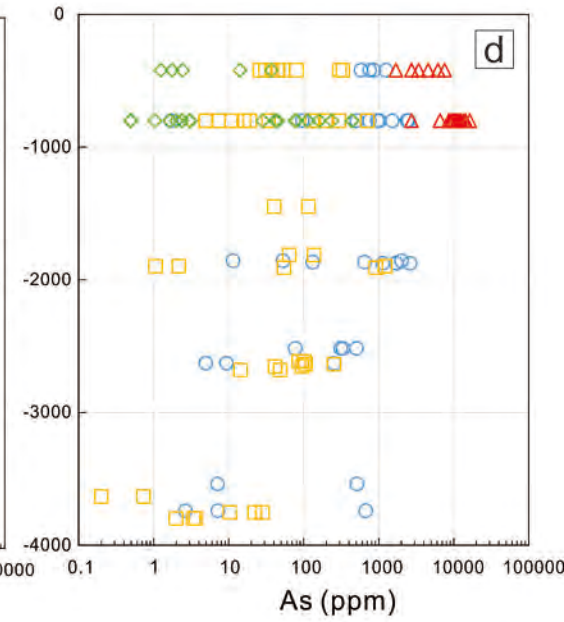
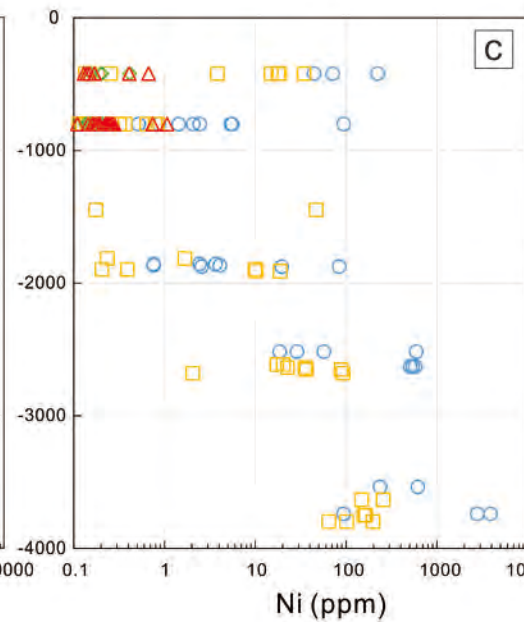
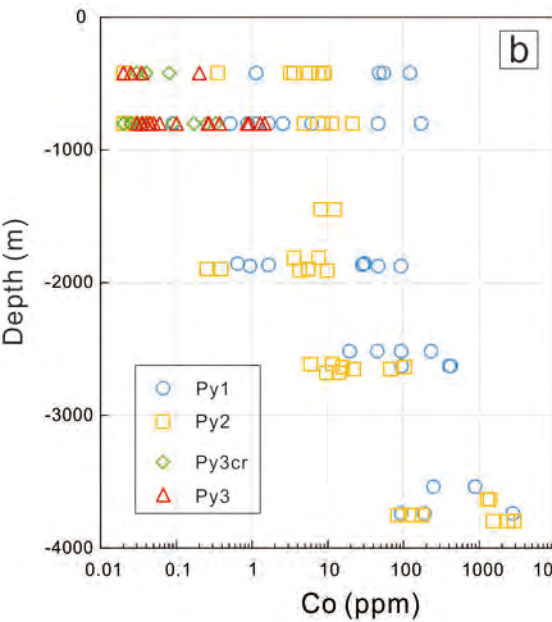
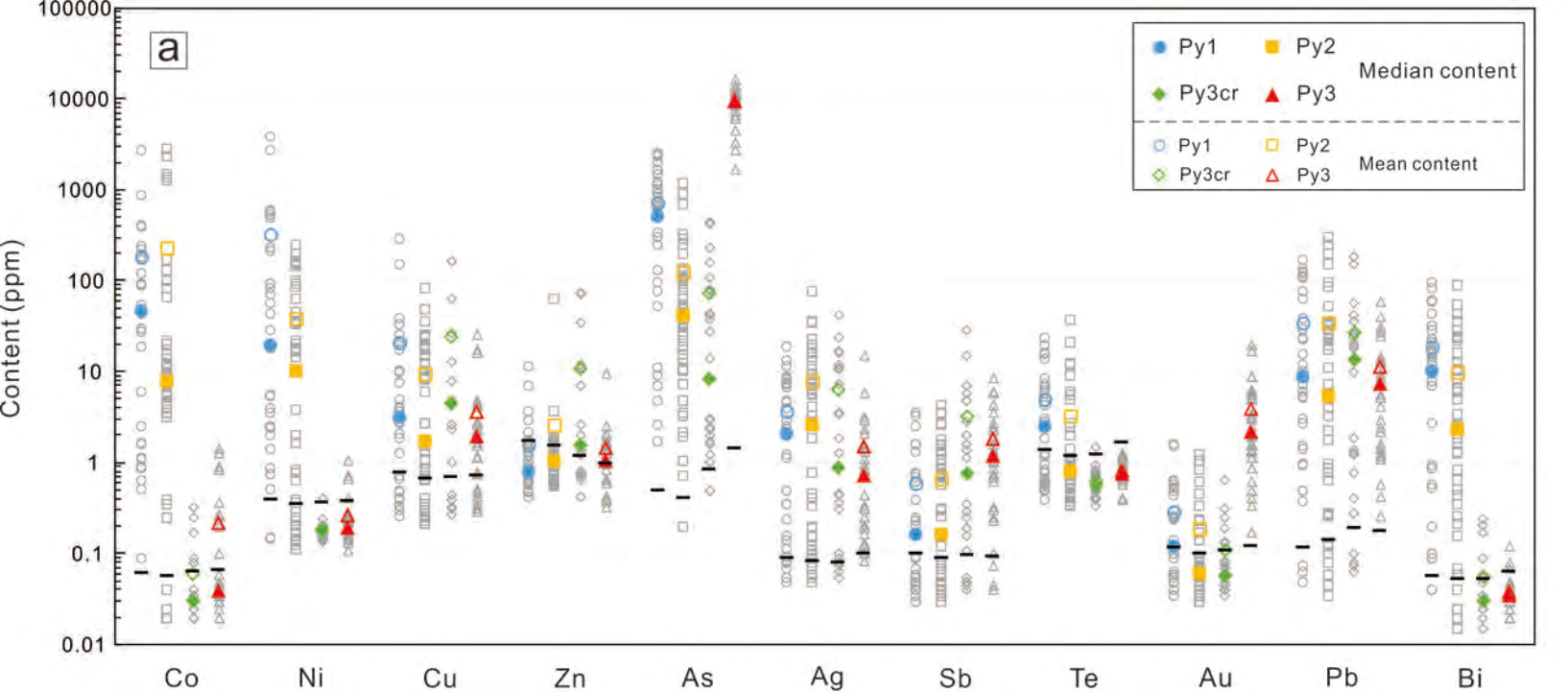


Fig. 5

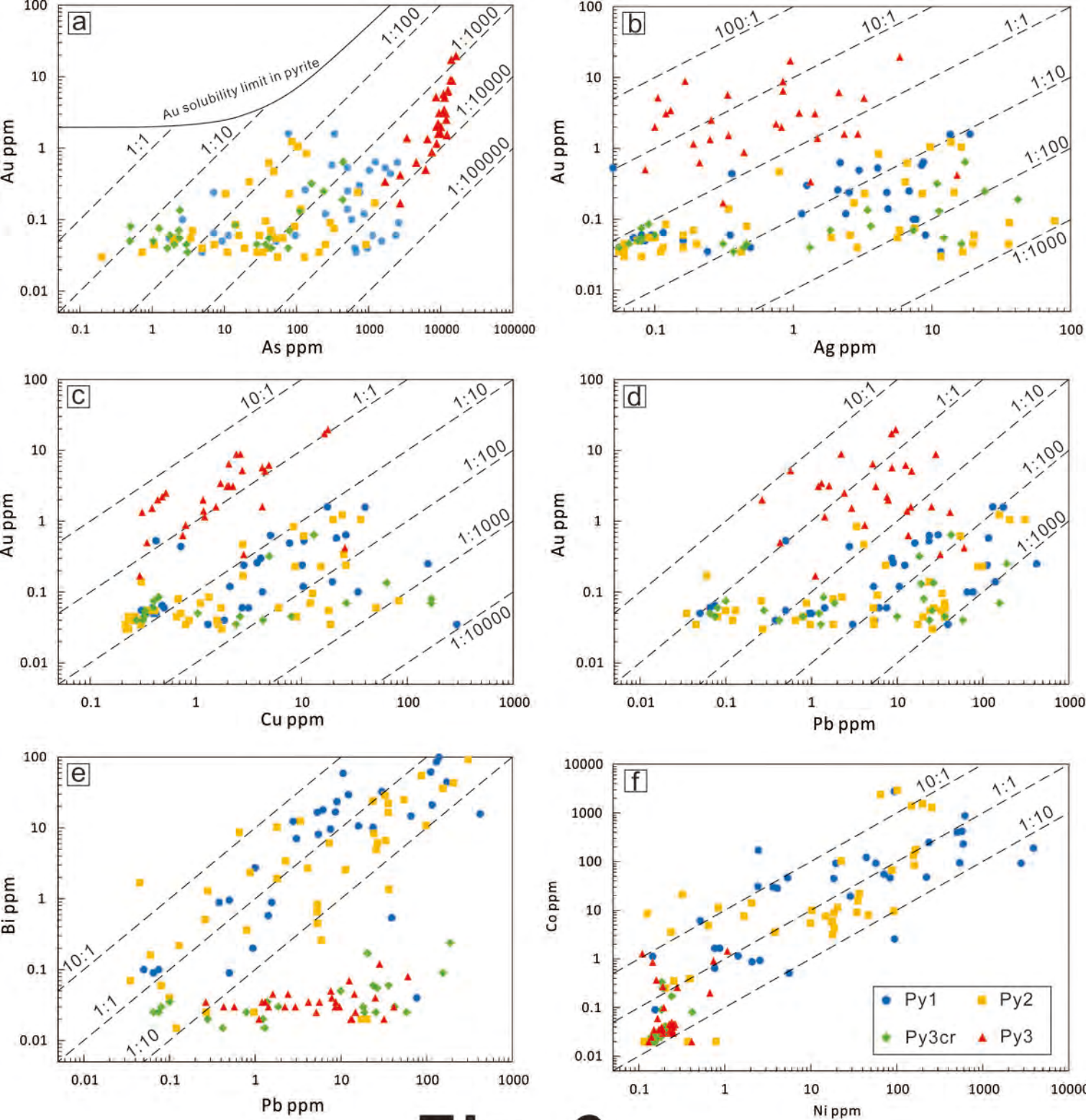


Fig. 6

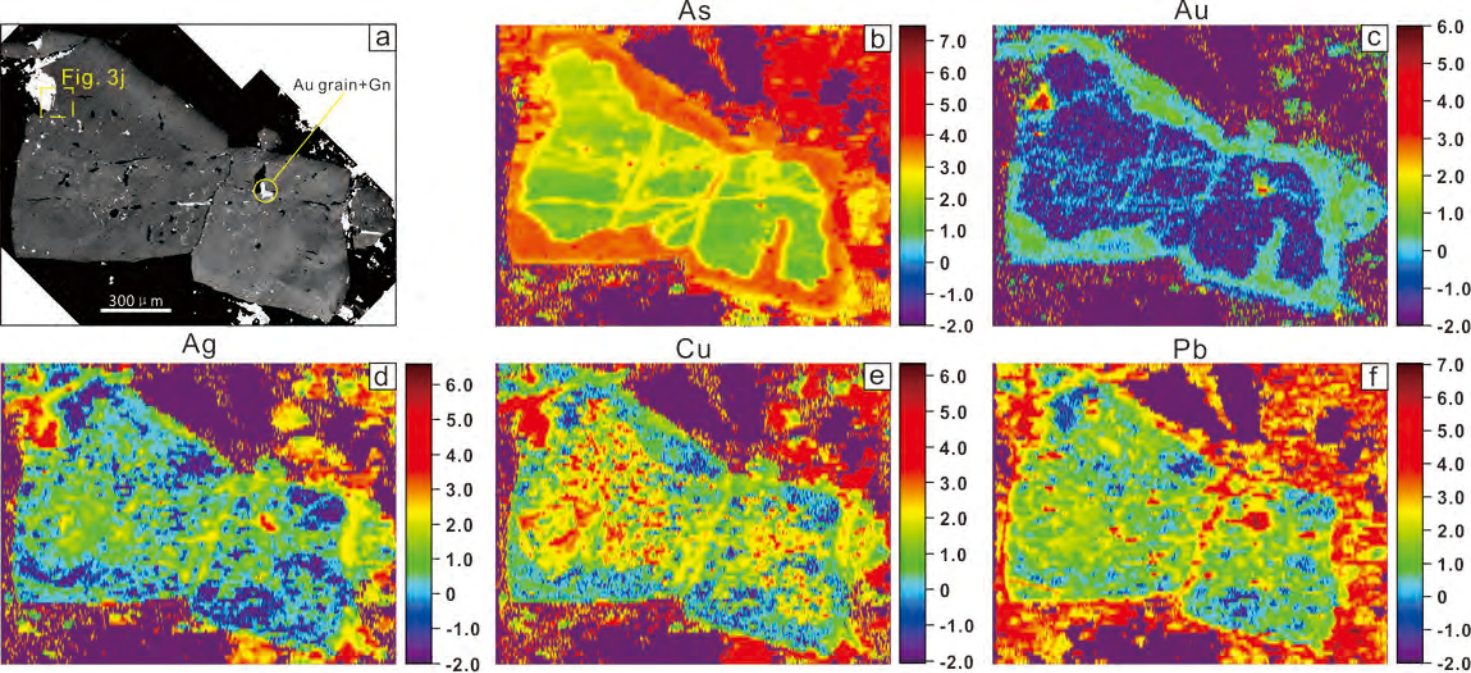


Fig. 7

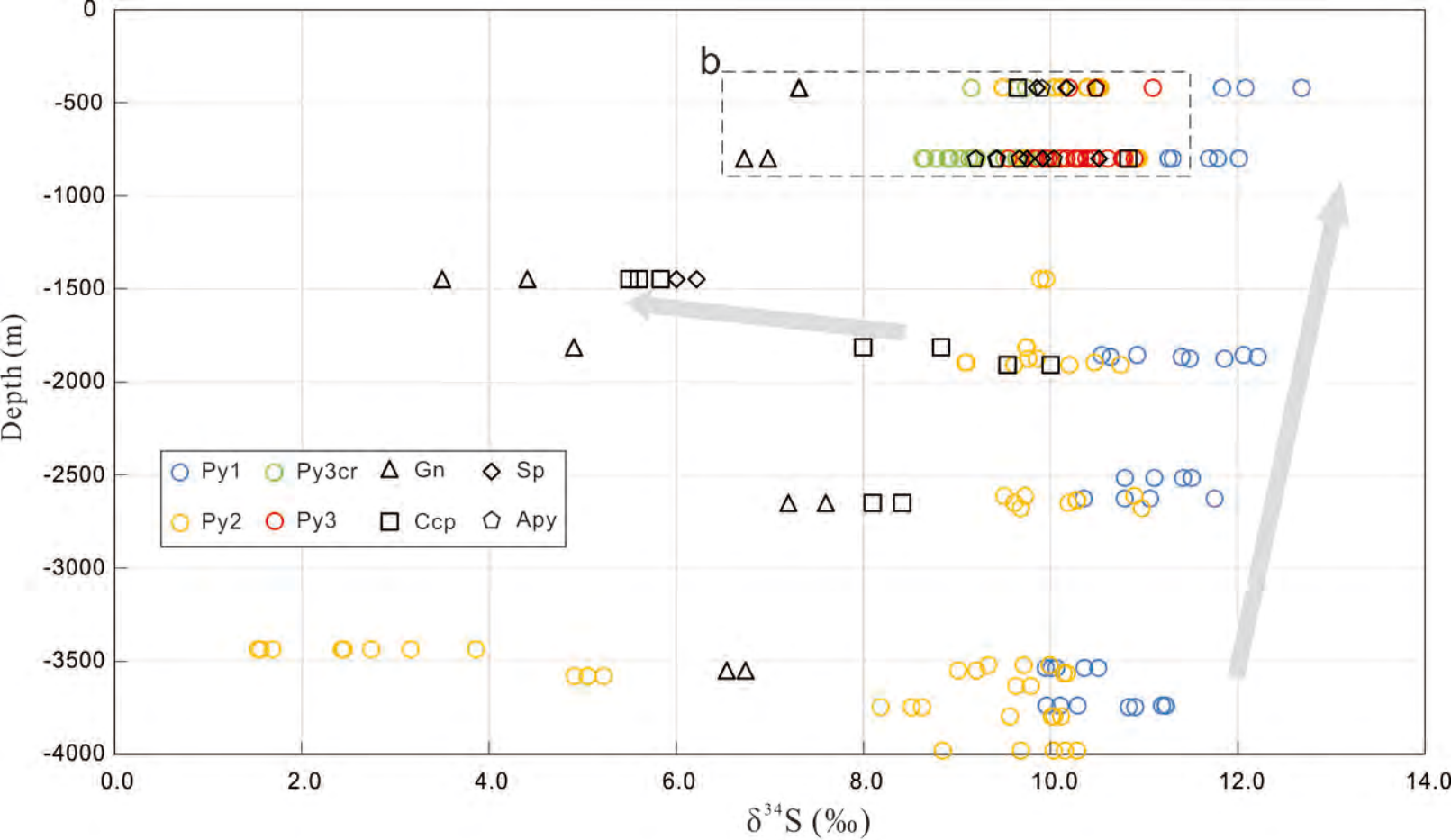


Fig. 8

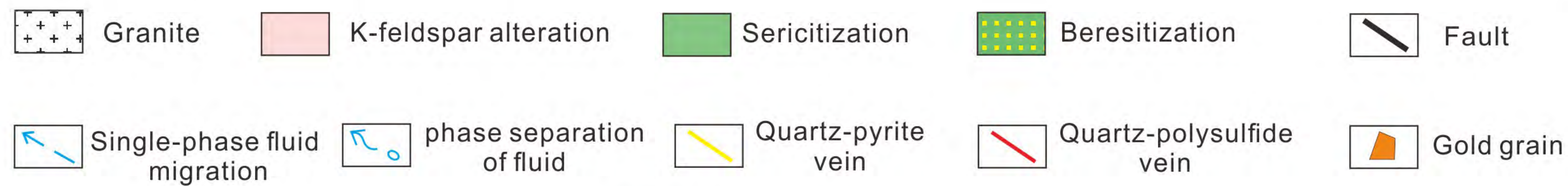
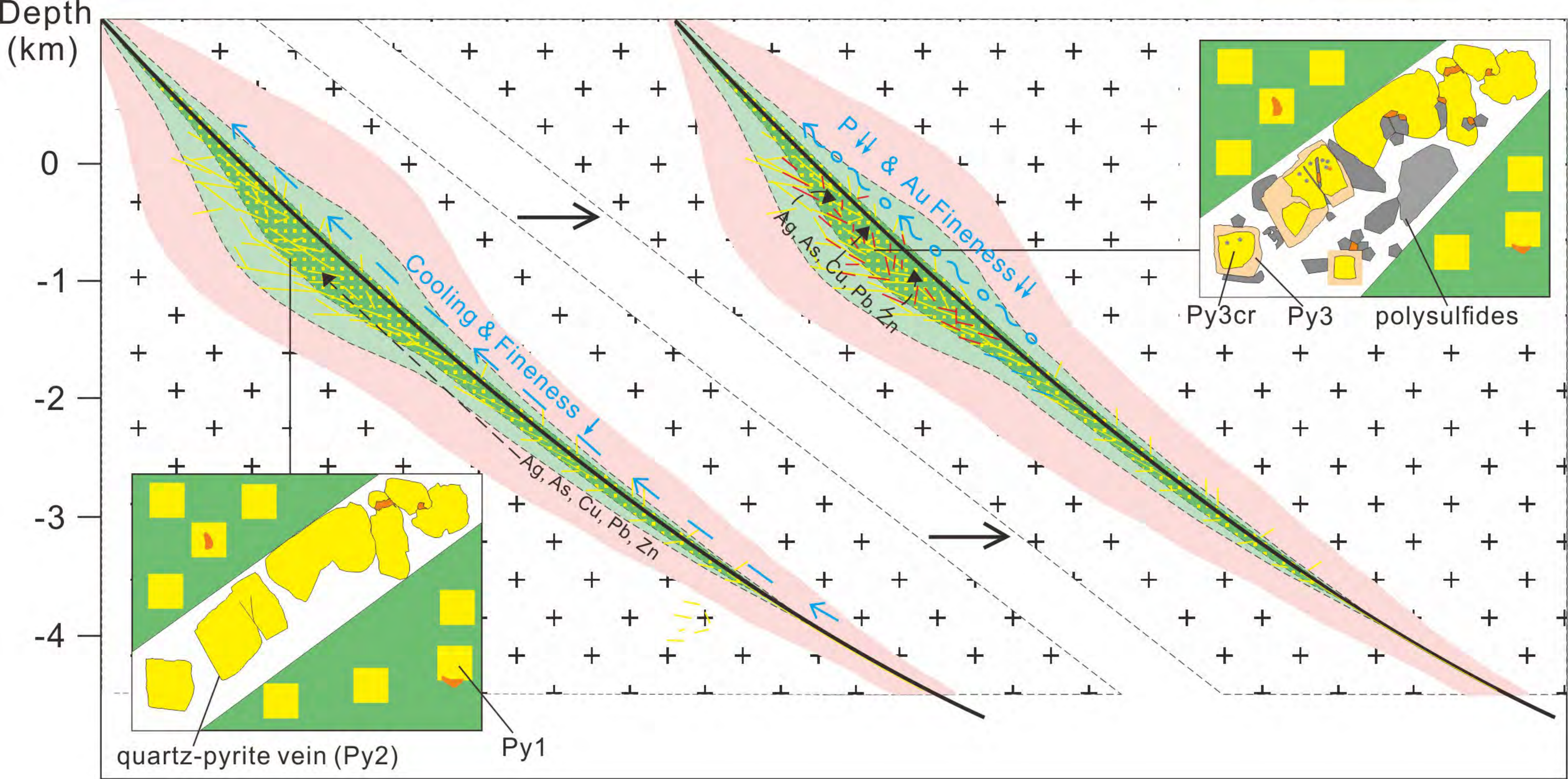


Fig. 9